Keio University

1858

CALAMVS GLADIO FORTIOR

Annual Report on Research Activities 2015

Tanabe Photonic Structure Group,

Department of Electronics and Electrical Engineering,

Faculty of Science and Technology, Keio University

Contents

Foreword

I am very thankful to everyone who is supporting our group, in the Department of Electronics and Electrical Engineering, in Keio University, Japan.

Since I started my lab five years ago, the number of members showed continuous growth and now we had five PhD students, nine master students, and five bachelors, in year 2015.

It was a fruitful year, in terms of constructing relationship and starting collaboration with other groups and researchers. Three of the PhD students have stayed for a half year in a lab abroad, Purdue University, Harvard University, and Freiburg University. Their stay have contributed to start connection with different groups abroad. As a result of such activities, along with our continuous effort, we managed to publish nine journal papers and 22 conference proceedings including two invited talks. I am very proud of my students, being keen on research activities and being very productive.

I have selected some of our research topics, and put them together to make this report. All of the manuscripts are written by the students, i.e. bachelors, masters and PhD students, and I basically did not made any correction. Therefore, I must admit that some are not well written, mainly due to the language problem. Even though, I am confident that the scientific contents provide important information and you may find interest in our research activities. I am appreciating and glad if you will give us any feedback to our researches.

August, 2016

Takasumi Tanabe, Associate Professor,
Department of Electronics and Electrical Engineering,
Keio University

Lab Members (Names and their positions after graduation)

Associate Professor: Takasumi Tanabe

Secretary: Naoko Kojima

PhD Students:

Nurul Ashikin Binti Daud	
	Continues her education in the graduate school of Keio University
Wataru Yoshiki	Continues his education in the graduate school of Keio University
	Leading Graduate School RA (all-round type)
Takumi Kato	Continues his education in the graduate school of Keio University
	Leading Graduate School RA (all-round type)
Ryo Suzuki	Continues his education in the graduate school of Keio University
	Leading Graduate School RA (global environment system leader)
Tomohiro Tetsumoto	Continues his education in the graduate school of Keio University
	Research associate (Keio University)

Master 2st Grade: (the class of 2013)

Tomoya Kobatake	Starts his carrier in industry
Sho Tamaki	Starts his carrier in industry
Zhelun Chen	Starts his carrier in industry
Yosuke Nakagawa	Starts his carrier in industry

Master 1st Grade: (The class of 2014)

Hiroki Itobe	Continues his education in the graduate school of Keio University
Yuta Ooka	Continues his education in the graduate school of Keio University
Yusuke Okabe	Continues his education in the graduate school of Keio University
Misako Kobayashi	Continues her education in the graduate school of Keio University
Takuma Nagano	Continues his education in the graduate school of Keio University

Bachelor 4th Grade: (The class of 2015)

Hajime Kumazaki	Continues his education in the graduate school of Keio University
Tomohisa Tabata	Starts his carrier in industry
Naoya Hirota	Continues his education in the graduate school of Keio University
Shun Fujii	Continues his education in the graduate school of Keio University
Atsuhiro Hori	Continues his education in the graduate school of Keio University

Research Activities

Reconfigurable high *Q* fiber coupled photonic crystal cavity formation

Tomohiro Tetsumoto (D1)

We achieved the formation of a reconfigurable high *Q* crystal cavity by bringing a tapered nanofiber into contact with a photonic crystal waveguide and obtained the highest *Q* of 6.7×10^5. We also obtained the highest coupling efficiency of 99.6% with a different radius nanofiber.

Key words: Photonic crystal nanocavity; Nanofiber; optical interface;

1. Introduction

Photonic crystal (PhC) nanocavities are prominent candidates as platforms for optical signal processing and quantum information technology. However, the coupling efficiency between optical fiber and PhCs is not usually high due to the mode mismatch between them. This study demonstrated the formation of a reconfigurable high *Q* cavity whose optical fiber coupling efficiency was almost 100%.

2. Cavity formation principle

We formed an optical cavity by bringing a tapered nanofiber into contact with a PhC waveguide. We call this cavity a fiber coupled PhC cavity (FCPC). This scheme was initially proposed by Yong-Hee Lee's group at KAIST for forming an optical cavity directly at a quantum dot in an InP PhC slab [1]. However, although theoretically its properties were very good, the experimentally obtained properties were not as high. This study employed a Si PhC waveguide to improve the properties.

The principle of cavity formation is as follows. The dispersion relation of the guided mode of a PhC waveguide is shown in Fig. 1(a). When the gap between a PhC waveguide and a nanofiber becomes small, the cutoff frequency of the guided mode moves downwards because of the change in the effective refractive index. This results in the localized formation of a mode gap, which functions as an optical cavity. We confirmed the formation of an optical cavity using the 3D FDTD method. We obtained a theoretical *Q* factor of 1.4×10^7 and a mode volume of $2.1(\lambda/n)^3$. The mode profile of the E_y mode is shown in Fig. 2(b).

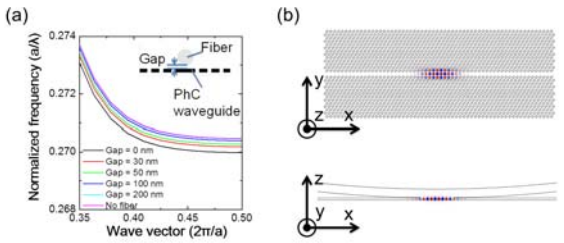

Fig. 1: (a) Dispersion relation of guided mode of PhC waveguide. (b) Ey mode profile of FCPC. [2]

3. Cavity formation experiment

Next, we performed a cavity formation experiment. The experimental setup is shown in Fig. 2(a). We prepared a dimpled tapered nanofiber with a radius of about 400 nm and brought it into contact with a W0.98 PhC waveguide. Then, we recorded the transmission spectrum. The highest *Q* factor we obtained was 6.7×10^5 (coupling efficiency (CE) of 6.6%) (Fig. 2(b)). We also obtained the highest CE of 99.6% ($Q = 6.1 \times 10^3$) with a different radius nanofiber (Fig. 2(c)). This value is the highest recorded CE for a PhC nanocavity and an optical fiber [2].

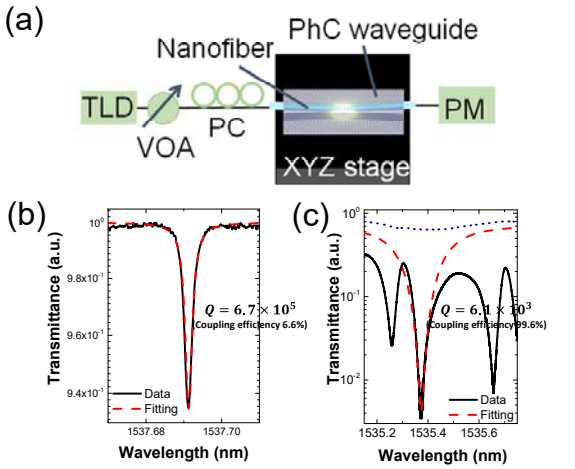

Fig. 2: (a) Experimental setup. (b) Resonant peak of highest Q mode. (c) Resonant peak of highest CE mode.

4. Resonant wavelength tuning

The tunability of the resonant wavelength is an important feature of FCPC. We demonstrated resonant wavelength tuning with the scheme shown in Fig. 3(a). We moved the xyz translation stage 100 nm downwards from the initial contact position. Because the nanofiber was fixed in position and adhered to the PhC waveguide as a result of electric static force, the contact area between the fiber and the PhC waveguide gradually decreased. This resulted in a decrease in the cavity length; thus, there was a blue shift of the resonant wavelength. The experimental result

is shown in Fig. 3(b). We obtained a tuning resolution of about 27 pm for each 100 nm downshift of the stage.

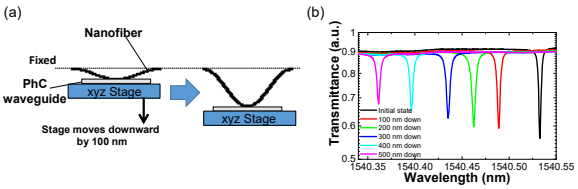

Fig. 3: (a) Schematic diagram of resonant wavelength tuning method. (b) Experimental result of resonant wavelength tuning.

5. Discussion of multi-resonant peaks

We obtained the multi-resonant peaks shown in Fig. 4(a). The free spectral range of these peaks was much shorter than that of a single PhC nanocavity with a length of 100 μm. This means these peaks were the result of multi-cavity formation along the PhC waveguide. To clarify the origin of these peaks, we observed the PhC structure using a scanning electron microscope and found that the waveguide surface was not perfectly flat (Fig. 4(a)). This should result in a small fluctuation in the effective refractive index along the waveguide, and so multiple cavities can be formed. In addition, we observed a string of bright spots along the waveguide when we input the light [into/in?] one resonant mode. This is one direct proof of multiple localizations at different positions. So, we believe that the multiple cavities formed an all-pass filter type coupled cavity that functions as an optical buffer.

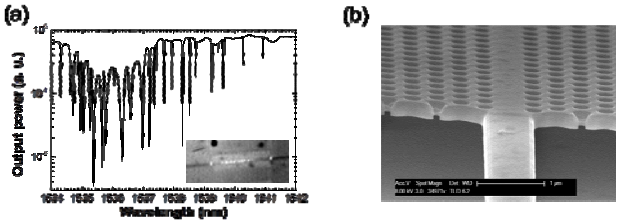

Fig. 4: (a) Obtained multi-resonant peaks. Inset shows multiple bright spots observed by infrared red camera. (b) Surface of PhC waveguide.

6. Summary

We formed an FCPC and obtained the highest Q of 6.7×10^5. We also achieved the highest CE of 99.6% with a different radius nanofiber. This is the highest recorded CE for a PhC nanocavity and an optical fiber. In addition, we demonstrated the tuning of the resonant wavelength of an FCPC. We also formed an all-pass filter type coupled cavity that consists of multiple cavities along a PhC waveguide. The FCPC platform is a potential way to achieve an effective input and output interface for light between an optical fiber and a PhC.

References

[1] M.-K. Kim, *et al*., *Opt. Express* **15**, 17241 (2009).
[2] T. Tetsumoto, *et al*., *Opt. Express* **23**, 16256 (2015).

Electro-optic modulator based on p-i-n integrated photonic crystal nanocavity fabricated with photolithography

Nurul Ashikin Binti Daud (D2), Tomohisa Tabata (B4), Yuta Ooka (M2), Tomohiro Tetsumoto (D1)

We report the first demonstration of an electro-optic modulator based on a photonic crystal (PhC) nanocavity with a *p-i-n* junction. Our device is fabricated with a photolithographic process, which is used in the complementary metal-oxide semiconductor (CMOS) process and can mass-produce devices. Moreover, the SiO_2 cladding of our device can also be realized in the CMOS process. We show that our device has a high-*Q* photonics crystal nanocavity ($Q = 1.4\times10^5$) and that we can change its refractive index by injecting carriers into the structure. Finally, we demonstrate GHz modulation based on the carrier plasma dispersion effect and the electro-optic property of this device showing a –3 dB cut-off frequency of nearly 1 GHz.

Key words: Silicon photonics, photonic crystal, optical modulator, width-modulated line defect photonic crystal nanocavity, carrier-plasma effect and all-optical switching.

1. Introduction

Silicon photonics has expanded the optical interconnect research field thanks to its low operating power, capacity for integration and the proficiency with which it can be combined with other existing silicon photonics devices. Silicon photonics is also the leading candidate for realizing optical interconnects due to its ease of combination with complementary metal-oxide semiconductor (CMOS) electronic fabrication technology [1], [2]. Therefore, an optical modulator that can be integrated in a CMOS chip has been intensively investigated [3]. A PhC nanocavity, which has a high quality factor (*Q*) and a small mode volume (*V*), has attracted many researchers [4]. A recent study showed that a photolithographically fabricated PhC nanocavity is compatible with CMOS [5].

This report summarizes our 2015 research in which we demonstrated an electro-optic modulator based on a *p-i-n* integrated photonic crystal nanocavity fabricated with a photolithographic process. We show that our results are similar to those previously reported for a photonic crystal nanocavity silicon modulator fabricated with an electron beam (EB) lithography process [6].

2. Device structure

Figure 1 shows a schematic illustration of our device. Input and output waveguides are coupled through barrier line defects whose width is W1.05. A cavity can be created by slightly shifting the center part of the waveguide air holes outwards. Shifting the air holes will increase the width of the waveguide at the center and that will lead to mode gap confinement and light will be confined. Figure 1 also shows the lattice constant *a*, hole radius *r* and slab thickness *t*. The size of the contact Al pad is 45 μm×25 μm. The parameters are w_i=2.9 μm, w_w=1.68 μm, w_c=8.9 μm and the doping density of the *p* and *n* regions are 9.5×10^9cm^{-3}, 5.7×10^9cm^{-3}, respectively.

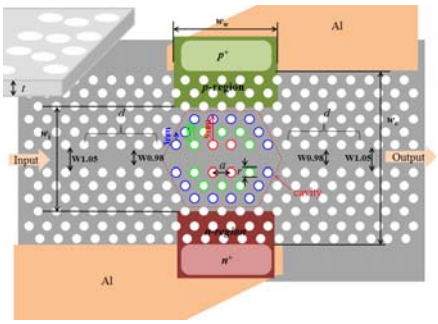

Fig. 1. Schematic illustration of device. The lattice constant *a*, hole radius *r* and slab thickness *t* are 420, 256 and 210 nm, respectively.

3. Spectrum characteristics

3.1 CW operation

Figure 2 shows the transmittance spectrum of the PhC nanocavity. A high *Q* of 1.4×10^5 is achieved at a wavelength of 1587.27 nm. The photon lifetime corresponds to 0.12 ns. The high *Q* is achieved by fabricating the PhC nanocavity with a photolithographic process.

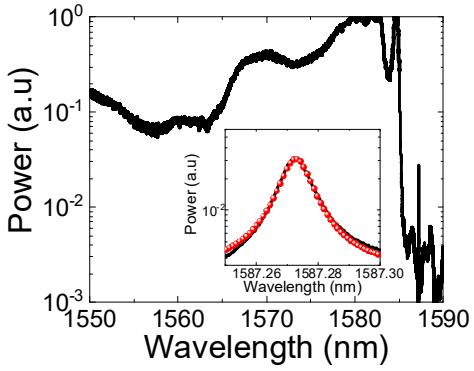

Fig. 2. Transmission spectrum when no voltage is applied at the electrodes. The inset shows Lorentzian fitting and the *Q* value is 1.4×10^5.

Next, forward and reverse bias DC currents are applied to the electrodes and the transmittance spectrum is measured with continuous wave (CW) laser light. The

results are shown in Figure 3. Figure 3(b) shows that the transmittance spectrum shifts to a shorter wavelength. By applying a forward bias voltage to the electrodes, carriers are injected into the structure and change the refractive index. As the voltage is increased, more carriers are injected into the structure. Therefore, the transmittance spectrum shifts to a shorter wavelength, which indicates that the modulation through the carriers is more dominant than caused by heat. However, Figure 3(c) shows that when more than 2.0 V is applied, the transmittance spectrum begins to shift to a longer wavelength region. This is due to the predominance of the thermo-optic effect in the device. At this stage, the thermo-optic effects dominate the carrier plasma dispersion.

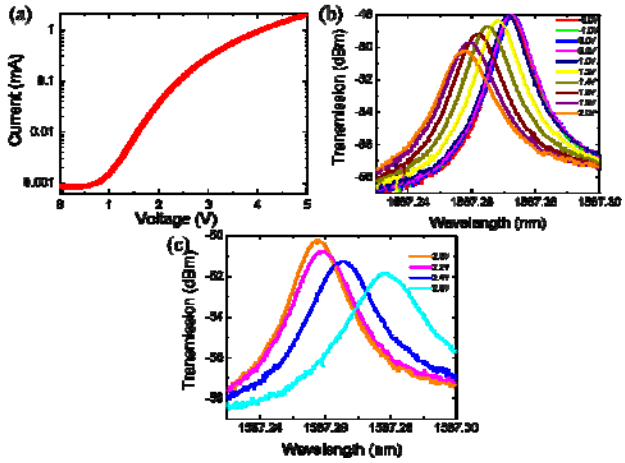

Fig. 3. Forward and reverse bias DC currents are applied to the Al pad of the device. n^+ is grounded and $+v$ is applied to the p^+. (a) An IV curve in the 0 V to 5.0 V range is applied. (b) The transmittance spectrum when reverse and forward bias voltage is applied to the electrodes. (c) The transmittance spectrum when excess voltage is applied.

There is no transmittance shift when less than 0 V (reverse bias voltage) is applied to the electrodes. This is because almost no current flows (Figure 3(a)) at a reverse bias voltage. The transmittance shows clear resonant shifts when 1.2 V is applied, which corresponds to a current flow of about 2.76 μA. We calculated the capacitance of this device using $C=\varepsilon_{si}S/d$ where $S = t\times w_w$, $d = w_i$ and ε_{si} is the dielectric constant of silicon. The capacitance is 5.88×10^{-18}, which is very small because this device is small.

3.2 Radio-frequency operation.

To measure the time average transmittance spectrum, we applied a rectangular pulse frequency signal generated by a pulse pattern generator to the electrodes. Note, we simultaneously performed the operation in the CW mode. A $\pm v$ voltage is applied to inject and extract carriers from the structure.

Figure 4 shows the results. The transmittance spectrum shows a clear shift to a longer wavelength. This is due to the longer injection of the carriers and makes them diffuse away from the *p-i-n* area. Therefore, the carrier extraction is inefficient at the electrodes, and carrier recombination around the cavity leads to a temperature increase. As a result, the transmittance spectrum shifts to a longer wavelength. A clear split peak can be seen when the voltage increases. This shows a to-and-fro cavity motion in the structure caused by applying $\pm v$ to the electrodes.

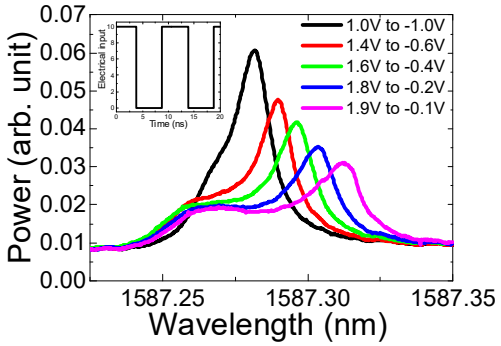

Fig. 3. Transmittance spectrum when 10 ns rectangular pulse is applied to the electrodes. The $\pm v$ value is shown in the graph legend.

4. Electro-optic modulation

Next, we demonstrate an electro-optic modulation. We observed an on-to-off and off-to-on modulation by tuning the wavelength to match the peaks of the transmittance spectrum, and the speed of the modulation range is 100 MHz to 1.0 GHz. Figure 5 shows the results.

The obtained results show that a GHz optical modulation is successfully demonstrated with a photolithographic PhC nanocavity integrated p-i-n junction.

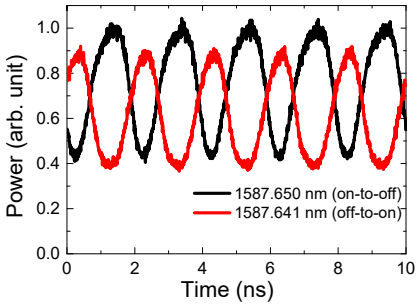

Fig. 5. (a) Output optical signal when 500 MHz frequency (2 ns rectangular pulse) is applied. The black and red lines indicate the input wavelengths. The red line shows an on-to-off modulation and the black line shows an off-to-on modulation.

Finally, we calculated the extinction ratio by measuring the modulation depth of each frequency. We obtained an electro-optic property for this device of almost 0.5 GHz.

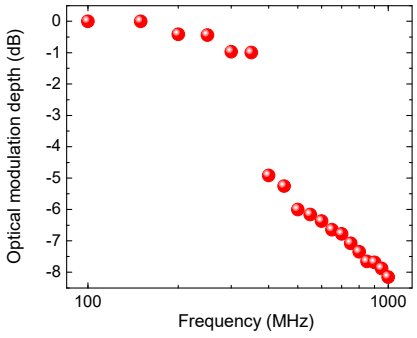

Fig. 6. Extinction ratio of device.

We strongly believe that we shall obtain a higher frequency bandwidth if we optimize the insulator width. As discussed above, the extremely small capacitance should allow even faster operation. This can be achieved if, for example we utilize the width of the *i* region and the depletion technique [7], [8].

5. Conclusion

We obtained a high *Q* with a photolithographically fabricated PhC nanocavity. We demonstrated a GHz modulation operation based on the carrier plasma dispersion effect and achieved a high-speed modulation in silicon. The operating power consumption can be reduced thanks to the large optical modulation. We believe that an even faster modulation operation could be obtained in the future by optimizing our device.

References

[1] G. Reed, G. Mashanovich, F. Gardes, and D. Thomson, “Silicon optical modulators,” *Nature photonics,* vol. 4, no. 8 Aug, 2010.

[2] Z.-Y. Li, D.-X. Xu, W. R. McKinnon, S. Janz, J. H. Schmid, P. Cheben, and J.-Z. Yu, “Silicon waveguide modulator based on carrier depletion in periodically interleaved PN junctions,” *Opt. Express*, vol. 17, no. 18, pp. 15947–58, 2009.

[3] Q. Xu, B. Schmidt, S. Pradhan, and M. Lipson, “Micrometre-scale silicon electro-optic modulator,” *Nat*. vol. 435, pp. 325-327, 2005.

[4] E. Kuramochi, M. Notomi, S. Mitsugi, A. Shinya, T. Tanabe, and T. Watanabe, “Ultrahigh-Q photonic crystal nanocavities realized by the local width modulation of a line defect,” *Appl. Phys. Lett.*, vol. 88, no. 4, p. 041112, 2006.

[5] Y. Ooka, T. Tetsumoto, A. Fushimi, W. Yoshiki, and T. Tanabe, “CMOS compatible high-Q photonic crystal nanocavity fabricated with photolithography on silicon photonic platform,” *Sci. Rep.*, vol. 5, p. 11312, 2015.

[6] T. Tanabe, K. Nishiguchi, E. Kuramochi, and M. Notomi, “Low power and fast electro-optic silicon modulator with lateral p-i-n embedded photonic crystal nanocavity.,” *Opt. Express*, vol. 17, no. 25, pp. 22505–13, Dec. 2009.

[7] H. C. Nguyen, Y. Sakai, M. Shinkawa, N. Ishikura, and T. Baba, “10 Gb/s operation of photonic crystal silicon optical modulators.,” *Opt. Express*, vol. 19, no. 14, pp. 13000–7, 2011.

[8] Y. Terada, H. Ito, H. C. Nguyen, and T. Baba, “Theoretical and experimental investigation of low-volgage and low-loss 25-Gbps Si photonic crystal slow light Mach-Zehnder modulators with interleaved p/n junction,” *Front. Phys.*, vol. 2, Nov, pp. 1–9, 2014.

Photonic crystal photo-receiver

Tomohisa Tabata (B4), Yuta Ooka (M1), Tomohiro Tetsumoto (D1)

We succeeded in making photonic crystal resonant with 2.2×10^5 by photolithography[1]. Photolithography is used in the complementary metal-oxide-semiconductor (CMOS) process and is suitable for mass production. Due to this, we demonstrated a photodetector using a photonic crystal nanocavity embedded with *p-i-n* junction fabricated with photolithography. A photodetector in the light element is important for a light detection and recently has become an attraction among the researchers. Thus far, it has proved impossible to manufacture a small footprint with a small dark current of photodetector. In this study, we demonstrated a photodetector based on silicon PhC nanocavity integrated with *p-i-n* junction fabricated by photolithography process. Our purpose is to realize a practical application by evaluating the performance of photodetector when a structure is manufactured via *p-i-n* junction embedded to a photonic crystal resonator by photolithography.

Keywords: silicon photonics, photonic crystal, photolithography, width change type microoptically resonant

1. Background

Photonic crystals (PhC) are generally easy to process and silicon is often used because the propagation loss is small. Silicon photonic crystal belongs to the field of silicon photonics. An aim of silicon photonics is to develop a technique for accumulating photo devices with various functions in one small chip. However, silicon is not effective in terms of, for example, receiving light. This is because silicon is transparent at telecom wavelength. Most researchers have attempted to use germanium[2] in silicon and ion implantation[3] to solve the problem. However, these structures pose problems in that they are difficult to manufacture, and high dark current due to presence of defect. A unified *p-i-n* structure in a waveguide has also been designed in order to employ two photon absorption (TPA), which has low coefficient[4]. However, difficulties include the fact that a high input light power is needed for this structure. A high *Q* PhC nanocavity is a good candidate because it allows to achieve a high photon density even with low input power. Previous study has demonstrated a high *Q* PhC nanocavity integrated with lateral *p-i-n* junction as a photodetector[5]. Due to the good crystal quality of silicon, it is able to reduce the value of dark current. This result constitutes great progress towards achieving a photodetector with high sensitivity and also to reduce the dark current. The *Q* value of this photodetector is 4.3×10^5. The responsivity value is 0.016 A/W. The dark current is 15 pA at -3 V. However, this photonic crystal is manufactured using EB lithography to realize high precision. Because the spot size is small, it takes a long time to manufacture, and this led to low productivity.

In this study, we demonstrate PhC nanocavity integrated with *p-i-n* junction fabricated by photolithography as photoreceiver. This report describes the work we undertook in 2015 to solve the above problem.

2. Design of Resonator

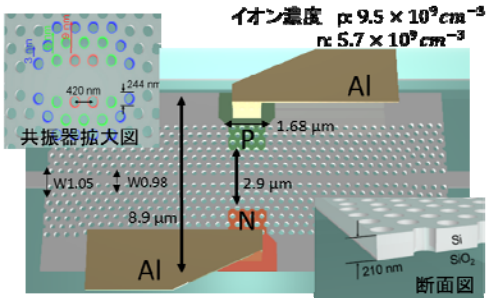

Figure 1. Design of photolithographically fabricated width modulated microcavity.

Figure 1 shows the schematic design of the device. This structure is called a width change type structure, and the resonator is manufactured by changing the width of part of the line defect waveguide of the photonic crystal. Previously, we had measured the value of *Q* factor of PhC nanocavity fabricated by photolithography[1] and we achieved the highest *Q* factor was 2.2×10^5. This proved that with photolithographic fabrication process, we able to achieve high *Q* factor which almost similar *Q* factor fabricated by EB lithography fabrication process. In this study, we show the transmittance spectrum in Figure 2. The *Q* value is 1.1×10^5, which is comparable with our previous measurement (2.2×10^5).

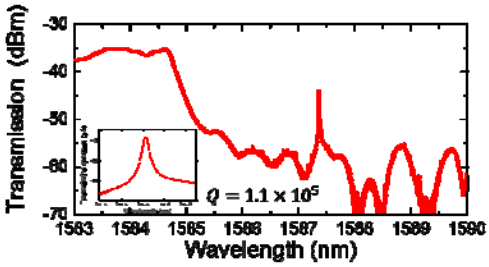

Figure 2. Transmittance spectrum of width change model photonic crystal resonator

3. Characteristic of photo-receiver

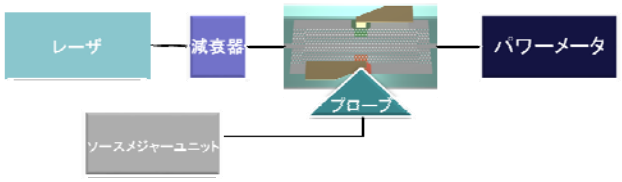

Figure 3. Experimental setup

Figure 3 shows the experimental setup. We measured the transmittance spectrum and the electric current generated by the resonator using a power meter and source measurement unit. The input optical power is 4.56 μW and the bias voltage is -3 V. The result show in Figure 4. Two-photon absorption occurs by constructing a resonator and confining a lot of light. This has led to the generation of photo-carriers. Thereby, the light can be detected as an electric current. In other words, the ideal performance of the photodetector is to find a high electric current when the resonator can confine a lot of light.

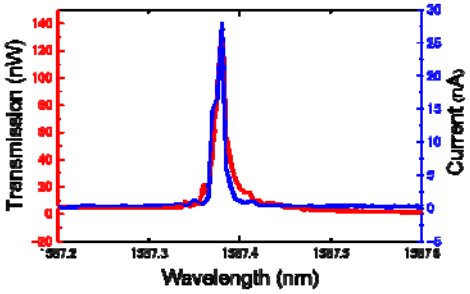

Figure 4. Transmittance spectrum (red line) and current value (blue line)

The detected current value almost agrees with the transmittance spectrum in Figure 4. This result shows that when a lot of light was confined in a resonator, two-photon absorption occurred, and an electric current was detected. This reveals its ability as a photodetector.

4. Responsivity

First, we describe light receiving sensitivity, which is an important index of the photodetector. We increased the input power from -35 dBm to 10 dBm and measured the current flow.

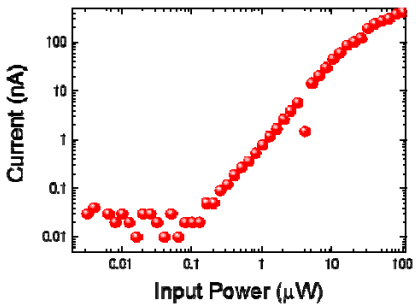

Figure 5. Responsivity

Figure 5 shows the result. The slope of this approximately straight line expresses the light receiving sensitivity. The light responsivity of this device was calculated in the 0.3~10 μW range and it shows that the value of responsivity is 0.0066 A/W. In comparison, the responsivity of PhC nanocavity device fabricated with EB lithography 41% higher than our device.

5. Smallest detection optical power

Next, we determine the smallest light detection strength. A plot in Figure 5 compares an input power of 0.1~0.3 μW. When the number of photons decreases, the excitation caused by the defect level decreases, and an electric current no longer flows. Thus, we take the approximate straight line of this range and consider the place where the y-axis (current value) becomes 0 to be the smallest detectable optical power. We were able to obtain the smallest detection optical power at 0.7244 μW. We believe that the resolving power of the ammeter is one of the causes for this. In addition, we believe that we can further reduce the light detection strength more if we can further reduce the dark current.

6. Summary

In a summary, this study shows that PhC nanocavity fabricated by photolithography can be used as a photodetector. However, compared to previous study EB lithography shows better characteristics of a photodetector. This is due to several factors. First, is the *Q* level of the device that we used this time. The *Q* level is only approximately a quarter compared to the one which was fabricated by EB lithography.
The responsivity can be increased 16-fold if the *Q* level can be quadrupled because a photodetector senses light by two-photon absorption. The second factor is coupling loss. With coupling, the component that we used this time has a loss of 4.3 dB. If this can be reduced, the input power could be increased and this would increase the light receiving sensitivity, and lead to an improvement in the quantum efficiency. The light receiving sensitivity can be increased 7.3 times if the coupling loss is zero.

References

1. Y. Ooka, T. Tetsumoto, A. Fushimi, W. Yoshiki and T. Tanabe "CMOS compatible high-Q photonic crystal nanocavity fabricated with photolithography on silicon photonic platform", Scientific Reports **5**, 11312 (2015).
2. T. Yin, R. Cohen, M. Morse, G. Sarid, Y. Chetrit, D. Rubin, and M. J. Paniccia, "31GHz Ge nip waveguide photodetectors on Silicon-on-Insulator substrate", Opt. Express **15**, 13965-13971 (2007).
3. M. Geis, S. Spector, M. Grein, R. Schulein, J. Yoon, D. Lennon, and T. Lyszczarz, "Silicon waveguide infrared photodiodes with >35 GHz bandwidth and phototransistors with 50 AW^{-1} response", Opt. Express **17**, 5193 (2009).
4. T. Liang, H. Tsang, E. Day, J. Brake, A. Knights, and M. Asghari, "Silicon waveguide two-photon absorption detector at 1.5μm wavelength for autocorrelation measurements", Appl. Phys. Lett. **81**, 1323 (2002).
5. T. Tanabe, H. Sumikura, H. Taniyama, A. Shinya, and M. Notomi "All-silicon sub-Gb/s telecom detector with low dark current and high quantum efficiency on chip", Appl. Phys. Lett. **96**,101-103 (2010).

Control and utilize the randomness in a photonic crystal

Yuta Ooka (M1), Nurul Ashikin Binti Daud (D2), Tomohiro Tetstumoto (D1)

We investigated the effect of randomness on photonic crystal waveguides and demonstrated an E/O modulator driven by random-based light confinement at a speed of 1 GHz. This study has an impact on photolithographic fabrication, because the fabrication error is larger with photolithography than with EB lithography. Moreover, the fabrication method has been shifting from EB lithography to photolithography. We employed photonic crystal waveguides with two different widths, namely W0.98 and W1.05. This structure enabled us to control the position at which confinement happens and the probability with which it occurs.

Keywords: Random photonic crystal, Silicon photonics, CMOS process, Line defect photonic crystal waveguide, E/O modulator, 2D FDTD

1. Background

Optical signal communication has been replacing electrical signal communication because its propagation loss and distortion are low. Silicon, which has a high refractive index (n = 3.47) in the communication band, is used as a material for optical devices. The research field dedicated to work on silicon optical devices is called silicon photonics. All-optical switches, E/O modulators and laser oscillators have already been realized based on ring resonators [1–3]. Photonic crystals (PhCs) are devices employed in silicon photonics. They have a structure consisting of periodic air holes in a slab. This structure makes it possible to confine light strongly in a small space thanks to Bragg reflection. Although both great confinement ability and much better devices can be realized, PhCs are vulnerable to fabrication error, namely randomness, because of their smaller structure. The transmittance of PhC waveguides (PCWGs), for example, decreases due to randomness and many related studies have been conducted. One study devised a method for calculating the transmission spectrum of PCWGs with randomness, and another study observed light transmission dependence on wavelength [4,5]. Although those studies focused on the physics of randomness, there are also studies that have focused on the practical side of randomness. In those studies, a quantum dot is embedded in a slab and laser emission occurs when light is localized at some point due to randomness [6]. However, the point at which randomness occurs and the emission direction cannot be predicted. There remain some problems to be solved before we can realize truly practical random PCWGs.

This report is about the work we undertook in fiscal 2015 to solve these problems. The result shows that randomness in PCWGs can be controlled at particular points and the probability of its appearance can also be controlled. As a result, we were able to demonstrate 1 GHz E/O modulation. Since there is a trend towards the photolithographic fabrication of PhCs [7], this work impacts strongly on PhC research.

2. Design of random PCWG

We employed the design shown in Fig. 1(a) to control both the confinement location and the probability of confinement appearing.

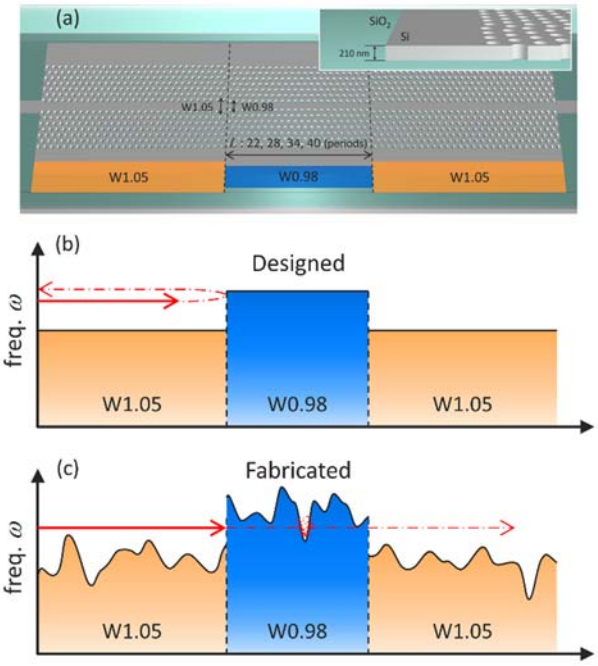

Fig. 1. (a) Schematic of device. (b), (c) Cutoff frequency and width of PCWGs. (b) Ideal structure. (c) Fabricated structure.

Figure 1(b), (c) show the relationship between cutoff frequency and PCWG width. These figures explain the principle of light confinement due to randomness. Transverse light is confined at W0.98 because a photolithographic PCWG has a certain amount of randomness. The appearance probability can also be controlled by changing the length, L, of W0.98.

3. Transmission spectrum

Figure 2 shows the transmission spectra of the PCWG structure described in the previous section. We performed a two-dimensional FDTD calculation [Fig. 2(a)] and measured an actual device [Fig. 2(b)]. 18 identical calculations and measurements were undertaken. Figure 2(a) [2(b)] shows a result of those calculations (measurements). The calculation considers a deviation of

2 nm in the air-hole position and diameter. And the length of W0.98 is 40 periods in both spectra.

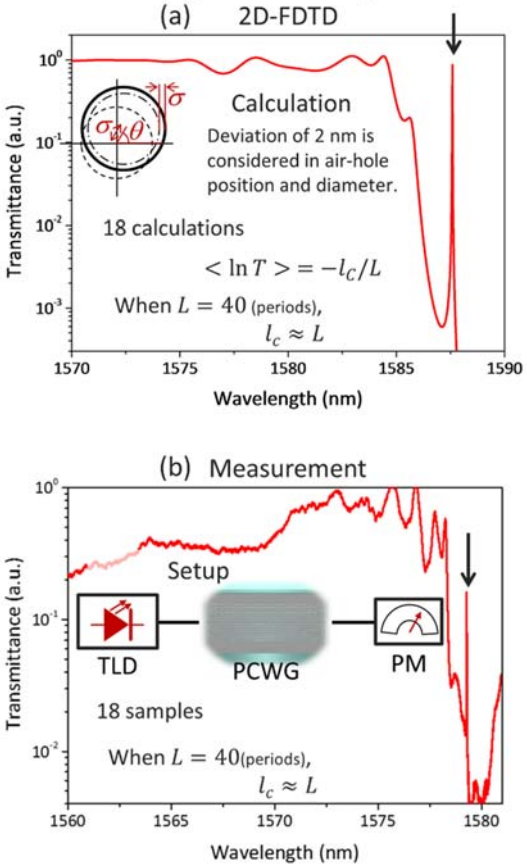

Fig. 2. Transmission spectrum of PCWG (a) calculated with 2D-FDTD, (b) fabricated with photolithography. The arrows in the figures correspond to confinement modes.

The mean free path, l_c, is defined as $< \ln T > = -l_c/L$. Using this equation, we calculated the relationship between l_c and L. And we found that $l_c \approx L$. Therefore, the randomness in the PCWG is in a diffusive regime.

4. Control of confinement mode

One of the objectives of this work is to control the light confinement position and the possibility of confinement appearing. Figure 3 shows light in a PCWG when the confinement mode is excited. Figure 3(a) shows the H_y component and Fig. 3(b) shows an IR camera image obtained from the top of the PhC slab. It is clear that light confinement occurs only in W0.98.

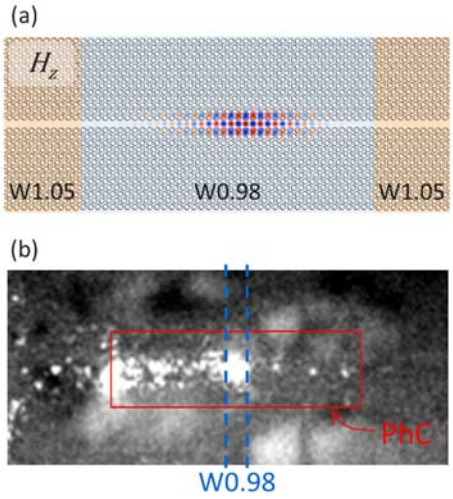

Fig. 3. Light confinement in W0/98. (a) Calculated mode profile of PCWG. H_y is displayed. (b) IR image taken from the top of the PhC slab when the light confinement mode is excited.

Next, we dealt with the probability of the appearance of light confinement. The relationship between the length of W0.98 and the Q-factor is shown in Fig. 4. As mentioned previously, we performed 18 identical calculations and measurements. We defined a peak as having a contrast between its apex and a background of 10 dB when it is fit with a Lorentzian. We can see that the probability of obtaining high Q peaks exceeds 80%. It shows that this PCWG can be put to practical use.

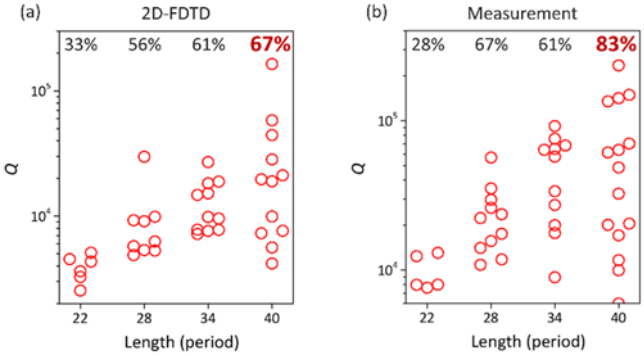

Fig. 4. Probability of confinement appearance. (a) Calculated with 2D-FDTD. (b) Measured result with photolithographic PCWG.

5. E/O modulator

Since light confinement occurs only in W0.98 and the yield exceeds 80%, we fabricated a p-i-n structure along W0.98, and demonstrated an E/O modulator. The basic PCWG structure is the same as that in previous reports. The p and n doping concentrations are shown in Fig. 5(a).

Figure 5(b) shows the setup for E/O modulation. A CW laser from a tunable laser diode (TLD) is modulated at a PCWG with a p-i-n junction, which is driven by an electric RF signal generated by a pulse pattern generator. The output is amplified with an erbium doped fiber amplifier (EDFA) and finally monitored with an optical sampling oscilloscope (OSO). The monitored result is shown in Fig. 5(c). It shows the potential of an E/O modulator at a speed of 1 GHz.

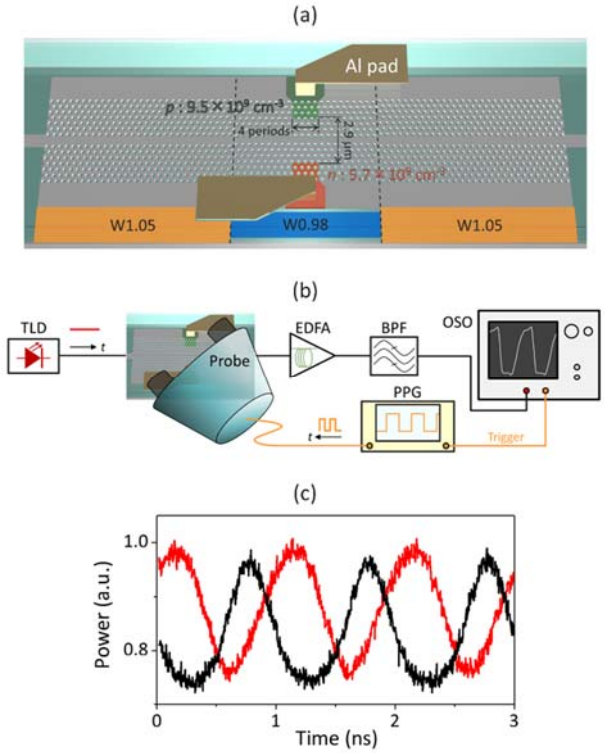

Fig. 5. (a) Schematic of PCWG used in this E/O demonstration. (b) Setup to demonstrate E/O modulation. (c) The monitored output when the speed is 1 GHz.

6. Conclusions

This study showed that the position and the probability of light confinement can be controlled with the combination of W0.98 and W1.05. We realized an E/O modulator operating at a speed of 1 GHz.

References

1. V. R. Almeida, C. A. Barrios, R. R. Panepucci, and M. Lipson, "All-optical control of light on a silicon chip," Nature **431**, 1081–1084 (2004).
2. Q. Xu, S. Manipatruni, B. Schmidt, J. Shakya, and M. Lipson, "12.5 Gbit/s carrier-injection-based silicon microring silicon modulators," Opt. Express **15**, 430–436 (2007).
3. H. Rong, S. Xu, Y.-H. Kuo, V. Sih, O. Cohen, O. Raday, and M. Paniccia, "Low-threshold continuous-wave Raman silicon laser," Nat. Photonics **1**, 232–237 (2007).
4. M. Patterson, S. Hughes, S. Combrié, N.-V.-Q. Tran, A. De Rossi, R. Gabet, and Y. Jaouën, "Disorder-induced coherent scattering in slow-light photonic crystal waveguides," Phys. Rev. Lett. **102**, 253903 (2009).
5. N. Le Thomas, H. Zhang, J. Jágerská, V. Zabelin, R. Houdré, I. Sagnes, and A. Talneau, "Light transport regimes in slow light photonic crystal waveguides," Phys. Rev. B **80**, 125332 (2009).
6. J. Liu, P. D. Garcia, S. Ek, N. Gregersen, T. Suhr, M. Schubert, J. Mørk, S. Stobbe, and P. Lodahl, "Random nanolasing in the Anderson localized regime," Nat. Nanotechnol. **9**, 285–289 (2014).
7. Y. Ooka, T. Tetsumoto, A. Fushimi, W. Yoshiki, and T. Tanabe, "CMOS compatible high-Q photonic crystal nanocavity fabricated with photolithography on silicon photonic platform," Sci. Rep. **5**, 11312 (2015).

Modeling of the modal interaction in a microcavity with LL equations

Tomoya Kobatake(M2)

We present a simulation model constructed of simultaneously formulated LL equations. It can be used for investigating the influence of the interference between different transverse modes on Kerr comb generation. We also calculate the model using the split-step Fourier method and use it to analyze the influence.

Key words: Optical frequency comb, Kerr comb, Nonlinear optics, Split-step Fourier method, LL equation

1. Introduction

An optical frequency comb is a spectrum that consists of equidistant lines similar to a comb in the frequency domain. Optical frequency combs are called “rulers of light” because of their high accuracy and stability. They are used as the optical frequency standard for spectroscopy. Moreover, we can expect them to be applied to large capacity optical communication, optical clocks, global positioning systems (GPS), and astronomical research [1]. Optical frequency combs are generated using a solid-state laser (Ti:sapphire laser) or a fiber laser. These lasers are problematic in that they are large, expensive, and need a lot of energy. Therefore, the number of studies related to the Kerr comb has increased in order to solve these problems [2]. A Kerr comb has a comb-like spectrum that is realized with a small size, low cost and low energy by using the nonlinear effect in a microcavity. In particular, many theoretical studies have revealed that Kerr combs become soliton state, which is characterized by low noise and a broad spectrum by controlling power and detuning [3][4]. On the other hand, these theoretical studies assume that there is only one mode in the cavity. However, there can be multiple modes simultaneously for example differently polarized modes, counter-propagating modes, and different transverse modes. They interact with each other, and the condition of Kerr combs will be influenced. In this study, we present a new calculation model by setting Lugiato-Lefever (LL) equations for each mode in a microcavity. Furthermore, we analyze the influence of the interaction on a Kerr comb by solving the model using the split-step Fourier method (SSFM).

2. Calculation model

A generalized mean-field LL equation is usually used to analyze the evolution of a Kerr comb in a microcavity [3].

$$t_R \frac{\partial^2 E}{\partial r^2} = \left(-\frac{\alpha}{2} - \frac{\kappa}{2} - i\delta_0 - \frac{iL\beta_2}{2}\frac{\partial^2}{\partial t^2} + iL\gamma\left|E\right|^2 \right) E + \sqrt{\kappa} S \tag{1}$$

where, t_R, r, α, κ, δ_0, L, β_2, γ and S are the round-trip time, the number of round-trips, intrinsic cavity loss, coupling loss, the detuning of the input wavelength, cavity length, the second order dispersion of the cavity, a nonlinear coefficient, and input driving power, respectively. We can calculate the electric field in the cavity by using the SSFM.

To simulate multi-mode behavior, we need to set the equation for each mode and add interaction terms. For example, when there are TE/TM modes (differently polarized modes), their electric fields Em and En can be calculated with Eq. (2).

$$t_R \frac{\partial^2 E_m}{\partial r^2} = \left(-\frac{\alpha_m}{2} - \frac{\kappa_m}{2} - i\delta_m - \frac{iL\beta_{m2}}{2}\frac{\partial^2}{\partial t^2} \right) E_m + iL\gamma_m\left(|E_m|^2 E_m + \frac{2}{3}|E_n|^2 E_m\right) + \sqrt{\kappa_m} S_m \tag{2}$$

The cross-phase modulation (XPM) term is added as the interaction between modes. In addition, we can easily develop the equations by adding other interactions such as four-wave mixing (FWM), Raman scattering, and linear coupling. Furthermore, we can solve Eq. (2) quickly by using the SSFM because Eq. (2) is based on an LL equation.

The mode profiles and dispersions of the TE/TM modes for calculations are shown in Fig. 1. They are calculated with FEM (COMSOL Multiphysics) and a toroidal microcavity is assumed.

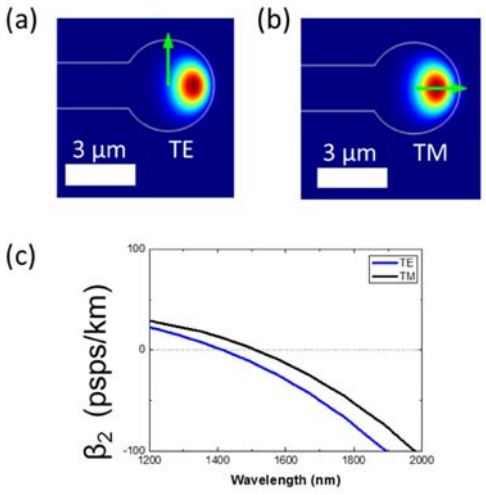

Fig.1: (a,b) Mode profiles of TE/TM modes. (c) Dispersions of TE/TM modes (blue/black).

3. Calculation result

We calculated the Kerr comb generation with Eq. (2), which included XPM for the TE/TM modes. Figure 2 shows the calculation result. The calculated temporal waveform and spectrum without XPM when we input the same power as for the TE/TM modes are shown in Fig. 2 (a). In this case, the degrees of the harmonics (= number of pulses) are different because the differences between the dispersions and the Kerr combs both increase. However, with XPM, as shown in Fig. 2 (b), the TE/TM modes are synchronized. When we consider the result in Fig. 2 (a), it appears that the modulation of the TE mode is induced by XPM from the TM mode comb. The TM mode is also synchronized with the TE mode when the input power to the TM mode is decreased as in Fig. 2 (c). These results show that we can control the status of the harmonics by controlling the input power.

Next, we show the calculated intracavity power when we tuned the input wavelength from shorter than the resonant wavelength to longer in Fig. 3(a). The ratio of the input power is S_1:S_2=1:0.4 and the input wavelength is the same for the TE/TM modes. The temporal waveform and the optical spectrum when it is blue detuned ((1) in Fig. 3(a)) are shown in Fig. 3 (b-1). The combs formed synchronized Turing patterns, which is the same as the state shown in Fig. 2. Figure 3 (b-2) shows the waveform and spectrum when the input wavelength is scanned to longer and red detuned from the resonant wavelength ((2) in Fig. 3(a)). This comb state is called a soliton state and it exhibits a narrow pulse, a broad spectrum and low RF noise. We can see the synchronized solitons as both the TE/TM modes. This is because of the XPM induced by the TE mode because the power of the TM mode is insufficient to generate a Kerr comb.

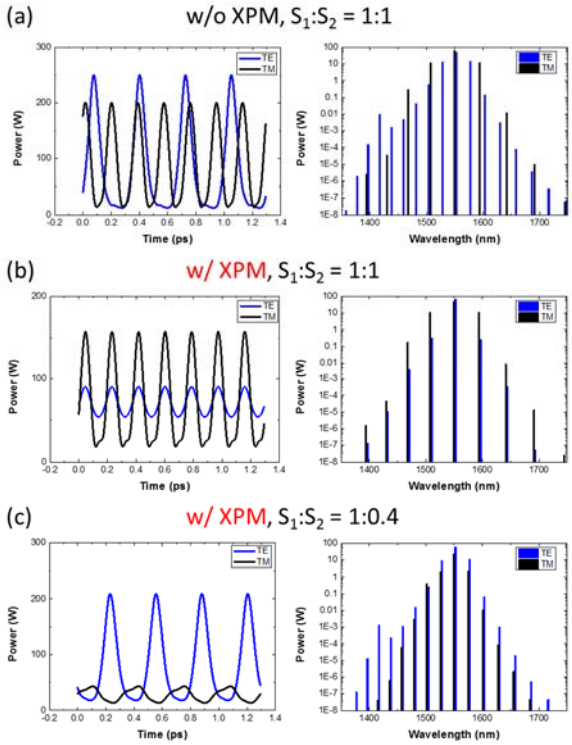

Fig. 2: Temporal waveforms (left) and optical spectrum (right). (a) Without XPM, S_1:S_2=1:1. (b) With XPM, S_1:S_2=1:1. (c) With XPM, S_1:S_2=1:0.4.

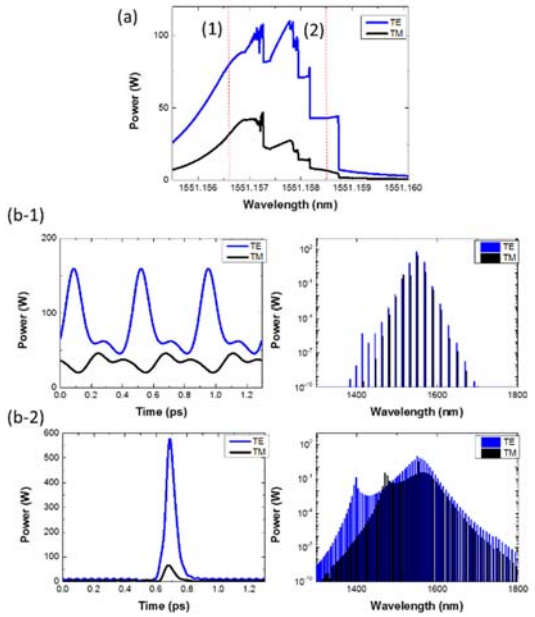

Fig. 3: (a) Input wavelength and intracavity power. (b-1) Temporal waveform and spectrum at (1) in Fig. 3(a). (b-2) Temporal waveform and spectrum at (2) in Fig. 3(a).

4. Conclusion

We constructed a new simulation model to calculate multi-mode Kerr comb generation by setting LL equations simultaneously and adding interaction terms. The calculation can be performed quickly by using SSFM. We also calculated the influence of XPM on Kerr comb generation with the model applied to the TE/TM modes. In this case, one mode synchronizes with the other mode due to XPM. Furthermore, we show that we can obtain solitons in both modes thanks to the XPM with a detuning method to generate solitons for a single mode. These results can help us to investigate a dual comb or dual soliton generated from a single microcavity.

References

[1] T. Udem, R. Holzwarth, and T. W. Hansch, Nature **416**, 233-237 (2002).
[2] P. Del'Haye, A. Schliesser, O. Arcizet, T. Wilken, R. Holzwarth, and T. J. Kippenberg, Nature **450**, 1214-1217 (2007).
[3] S. Coen, H. Randle, T. Sylvestre, and M. Erkintalo, Opt. Lett. **38,** 37 (2013).
[4] C. Godey, I. Balakireva, A. Coillet, and Y. Chembo, Phys. Rev. A **89**, 063814(2014)
[5] T. Herr, V. Brash, J. Jost, C. Wang, N. Kondratiev, M. Gorodetsky, and T. Kippenberg, Nature Photon. **8**, 145-152 (2014)

Broad bandwidth visible comb generation via third-order optical nonlinearity

Akitoshi Chen-Jinnai (M2)

Kerr comb generation using microcavities in the visible range has been limited by strong material dispersion. In this study, we utilize third-order optical nonlinearity. A Kerr comb in the infrared range undergoes the third harmonic generation (THG) process and the third-order sum frequency generation (SFG) process, which produces a set of optical comb lines in the visible range (visible comb). In this way, we demonstrated broad bandwidth visible comb generation from a single wavelength continuous-wave (CW) pump laser in a silica toroid microcavity.

Key word: Microcavity, Optical frequency comb, Third-order optical nonlinearity, Stimulated Raman scattering

1. Introduction

An optical frequency comb is a spectrum that consists of equidistant lines similar to a comb in the frequency domain. We can use an optical frequency combs as a rulers for measuring optical frequency with high precision. Therefore, optical frequency combs are expected to be applied to spectroscopy, optical clocks and global positioning systems (GPS). Optical frequency combs are generated using a solid-state laser or a fiber laser, however these lasers are large, expensive and need a lot of energy. Kerr comb generation with microcavities has been proposed as a way of solving these problems [2].

Kerr combs are generated from many types of microcavities, for example silica toroid, excimer grade calcium fluorite (CaF2) and silica disk microcavities [2-4]. Even though an optical comb in the visible region (visible comb) is expected to be applied to bioimaging, every study related to Kerr comb generation has reported on Kerr combs generated in the infrared region by an infrared pump laser. There have been no reports about Kerr comb generation in the visible region. This is because microcavities in the visible range have strong normal dispersion resulting from the material properties. Therefore, some researchers have generated a visible comb by converting an infrared Kerr comb into a visible comb instead of generating a Kerr comb in the visible region [5].

In this study, we use a silica toroid microcavity to generate visible combs. We convert an infrared Kerr comb into a visible comb via third-order optical nonlinearity. Additionally, we generate a broad bandwidth visible comb by converting an infrared Kerr comb and a Raman wave.

2. Experimental setup

An infrared Kerr comb is generated via four-wave mixing (FWM) by coupling a single wavelength, continuous-wave (CW) infrared laser to a microcavity. We convert infrared Kerr comb lines into a set of visible comb lines via third harmonic generation (THG) and third-order sum frequency generation (SFG). The visible comb bandwidth is limited by the original optical comb. To generate a visible comb with a broad bandwidth, we also convert Raman wave produced stimulated Raman scattering (SRS).

We use a silica toroid microcavity, which has both a high quality factor (Q) and broad Raman gain. Therefore, a Raman wave can be easily produced in a silica toroid microcavity, and a high order Raman wave can also be produced far from the pump wavelength via cascade Raman scattering [6]. We try to convert an infrared Kerr comb and a Raman wave into their visible counterparts so that a visible comb has a broad bandwidth.

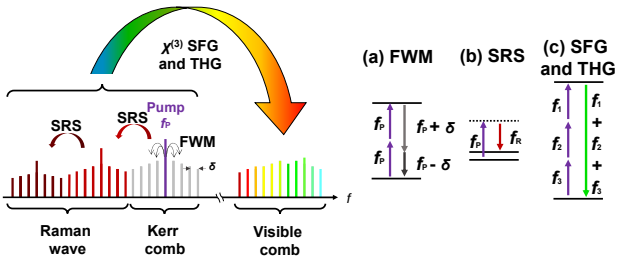

Fig. 1: In a silica toroid microcavity, a Kerr comb and a Raman wave are generated by four wave mixing (FMW) and stimulated Raman scattering (SRS). A visible comb is produced by converting a Kerr comb and a Raman wave via third harmonics generation (THG) and third-order sum frequency generation (SFG).

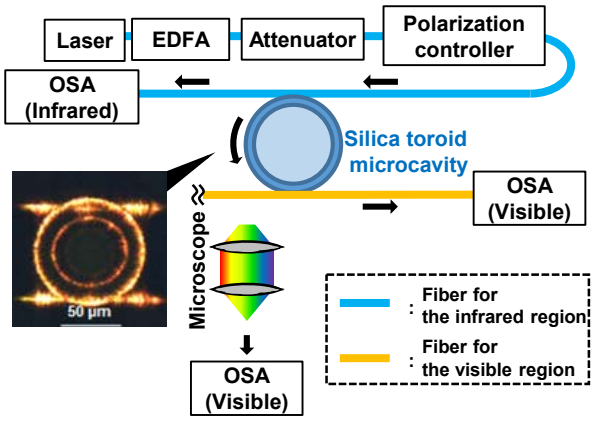

Fig. 2: In our experimental setup, we use two tapered fibers to couple a silica toroid microcavity. One is for pumping and measuring the infrared region light, and the other is for measuring visible light. The visible light can also be measured via a microscope without a fiber.

Figure 2 shows our experimental setup. A CW infrared laser (line width: 100 kHz) is amplified by an erbium-doped fiber amplifier (EDFA), and then the pump laser is coupled to a silica toroid microcavity by a tapered fiber (thickness: 1 μm). The pump wavelength is tuned toward the long wavelength side to generate a Kerr comb and a Raman wave. A visible spectrum can be measured with a visible spectrum analyzer via both a microscope and a fiber.

3. Experimental results

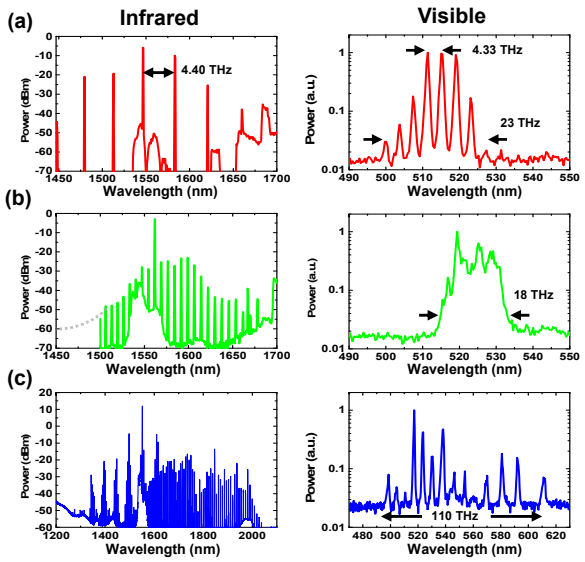

Fig. 3: The left spectra are for the Kerr comb and Raman wave in the infrared region. The right spectra are for the visible comb measured via a microscope.

We use the setup shown in Fig. 2 to measure comb spectra in the infrared and visible regions. (Fig. 3). We used a silica toroid microcavity with a Q factor of about 10^7, and with major and minor diameters of 50 and 13 μm, respectively. The pump wavelength and power, respectively, are 1545.9 nm and 0.94 W in Fig. 3(a), 1560.9 nm and 1.14 W in Fig. 3(b), and 1551.6 nm and 1 W in Fig. 3(c). In Fig. 3(a), the interval of the Kerr comb lines is 4.4 THz, and the interval of the visible comb lines is 4.33 THz. In Fig. 3(b), the Kerr comb lines are 1-FSR (FSR: free spectrum range), and the interval of the visible comb lines is also changed. The intervals of the Kerr comb lines and visible comb lines substantially match. Accordingly, we demonstrate that the interval of the visible comb lines can be controlled by modifying the interval of the Kerr comb. In Fig. 3(a) and (b), the Raman wave is not produced from the microcavity, and the visible comb bandwidths are 23 and 18 THz, respectively. To measure a visible comb when a Kerr comb and a Raman wave are generated at the same time, we change the input wavelength and the coupling efficiency between the microcavity and the tapered fiber. Figure 3(c) is the result, and shows not only a Kerr comb but also a Raman wave converted by cascade Raman scattering. A broad Raman wave is produced on the long wavelength side, and the visible comb also spreads on the same side. With Fig. 3(c), we demonstrate the generation of a visible comb, whose bandwidth is 110 THz extending from 498 to 612 nm.

4. Conclusion

Although Kerr comb generation is disturbed by strong material dispersion in the normal dispersion regime, we generated a visible comb by converting an infrared Kerr comb into the visible via THG and SFG in a silica toroid microcavity. In this study, we also succeeded in generating a broad bandwidth visible comb (110 THz) by converting a Kerr comb and Raman wave by cascade Raman scattering.

References

[1] Th. Udem, R. Holzwarth, and T. W. Hänsch, Nature **416**, 233-237 (2002).
[2] P. Del'Haye, A. Schliesser, O. Arcizet, T. Wilken, R. Holzwarth, and T. J. Kippenberg, Nature **450**, 1214-1217 (2007).
[3] I. S. Grudinin, N. Yu, and L. Maleki, Opt. Lett. **34**, 878-880 (2009).
[4] X. Yi, Q.-F. Yang, K. Y. Yang, M.-G. Suh, and K. Vahala, Optica **2**, 1078-1085 (2015).
[5] S. Miller, K. Luke, Y. Okawachi, J. Cardenas, A. L. Gaeta, and M. Lipson, Opt. Express **22**, 26517-26525 (2014).
[6] T. J. Kippenberg, S. M. Spillane, B. Min, and K. J. Vahala, IEEE J. Sel. Top. Quantum Electron. **10**, 1219-1228 (2004).

Suppression of cavity optomechanical oscillation for phase-locked Kerr comb generation

Ryo Suzuki (D1)

Silica toroid microcavities have a high quality factor (Q) and a small mode volume, which makes them suitable as Kerr comb sources. However, cavity optomechanical oscillation disturbs Kerr comb generation with phase-locking and soliton state. In this study, we demonstrated phase-locked comb generation from a toroid microcavity by suppressing the oscillation.

Key words: Microcavity, Optical Frequency Comb, Mode Locking, Cavity Optomechanics

1. Introduction

Optical frequency combs have lines with equal intervals in the frequency domain with a large bandwidth and are suitable for such applications as precise frequency measurement, spectroscopy, optical communication and astronomy. In 2005, T. W. Hänsch and J. L. Hall won the Nobel Prize for their contribution to developing precise metrology with a frequency comb. Although the comb source consists of a Ti:sapphire laser or fiber laser, it is large and expensive. Therefore, frequency comb generation from a microcavity has been studied to realize a compact, low cost source with a low power consumption. A comb generated from a microcavity is called a Kerr comb.

Recently, Kerr combs with phase-locking and soliton state have been attracting a lot of attention. The pulse generation has been demonstrated using a magnesium fluoride crystal, silicon nitride ring and silica disk microcavities. However, a silica toroid microcavity, which has a high Q and a small mode volume, is not much used in pulse generation research. One reason for this is that cavity optomechanical oscillation makes Kerr comb noisy. Here, we demonstrate phase-locked comb generation from a toroid microcavity by controlling the pump wavelength.

2. Cavity optomechanics

Cavity optomechanics is the interaction between light and matter to exchange energy, whose basic model with a cavity and a spring is shown in Fig. 1(a). With ring-type cavities such as toroid microcavities, the structure oscillates in the radial direction when coupling the light (Fig. 1(b)). The displacement of the effective cavity length caused by oscillation modulates the input and output lights. The oscillation is amplified or suppressed depending on the detuning between pump and resonance. In this research, we controlled the pump light to suppress the oscillation.

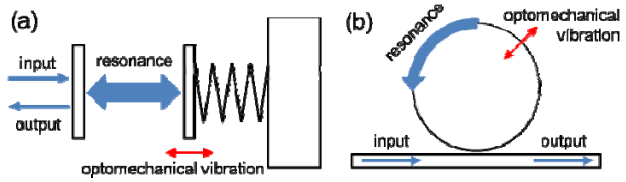

Fig. 1: Model of cavity optomechanics. (a) Fabry-Perot cavity. (b) ring cavity.

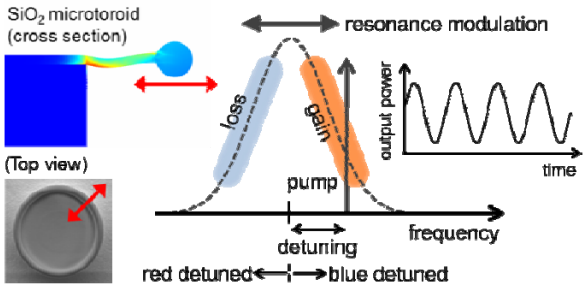

Fig. 2: Direction of optomechanical oscillation with toroid microcavity (left) and output light modulation (right). The oscillation is amplified and suppressed when the pump is blue and red detuned, respectively.

3. Experimental results

We generated a Kerr comb using a toroid microcavity with an optical Q of 10^7, a mechanical Q of 2.5×10^3, a cavity FSR of 963 GHz and a mechanical eigen-frequency of around 60 MHz. Continuous wave light at 350 mW is coupled with the resonance through a tapered fiber by scanning from a short to a long wavelength. Figure 3 shows the transmittance, optical spectra and radio frequency (RF) signals detected with a photodiode. Although there are multiple 60 MHz RF signals at state-1, 2 and 3, which are caused by optomechanical oscillation, these peaks disappear at state-4.

Next, we measured the autocorrelation waveforms. Figure 4(a) shows the autocorrelation waveforms for state-3 and state-4. The blue dots and green lines are measurement results and transform limited pulses (TLPs) calculated from the spectra, respectively. At state-4, the measurement result corresponds to the TLP. In addition, we measured the linewidth of the comb line next to the pump. Although at state-3 the signal was not measured clearly, at state-4 a narrow linewidth was observed, which is the same order as those of the pump and reference lasers. Hence, these results show that phase locking can be achieved in a toroid microcavity.

4. Conclusion

Toroid microcavities are prone to optomechanical oscillation, that makes generated Kerr comb noisy. Here, we generated a phase-locked Kerr comb by controlling the pump wavelength. The linewidth of the comb line next to the pump is narrow and is of the same order as those of the pump and reference lasers.

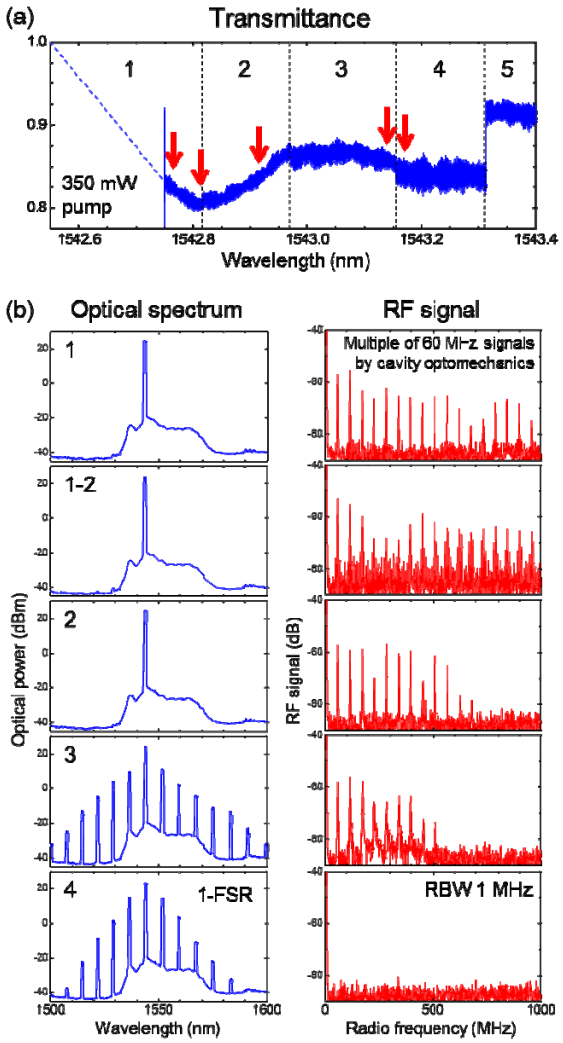

Fig. 3: (a) Transmittance change when scanning the pump wavelength from a short to a long wavelength. At state-5 and the dotted line in state-1, the pump couples into another resonance, which is used for Kerr comb generation. (b) Optical spectra and RF signals detected by photodiode. The RF signal with multiples of 60 MHz comes from the oscillation.

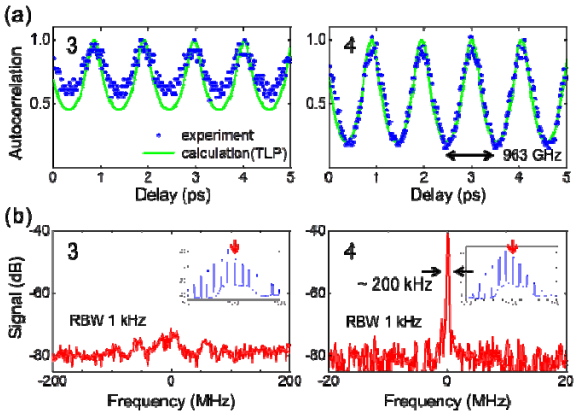

Fig. 4: (a) Autocorrelation waveforms of measurement (blue dots) and TLP (green line) at state-3 (left) and state-4 (right). (b) Linewidth of comb line next to pump.

References

[1] Th. Udem, R. Holzwarth, and T. W. Hänsch, Nature **416**, 233-237 (2002).

[2] P. Del'Haye, T. Herr, E. Gavartin, M. L. Gorodetsky, R. Holzwarth, and T. J. Kippenberg, Phys. Rev. Lett. **107**, 063901 (2011).

[3] T. J. Kippenberg, R. Holzwarth, and S. A. Diddams, Science **332**, 555-559 (2011).

[4] T. Herr, V. Brasch, J. D. Jost, C. Y. Wang, N. M. Kondratiev, M. L. Gorodetsky, and T. J. Kippenberg, Nature Photon. **8**, 145-152 (2014).

[5] X. Yi, Q.-F. Yang, K. Y. Yang, M.-G. Suh, and K. Vahala, Optica **2**, 1078-1085 (2015).

[6] T. Carmon, H. Rokhsari, L. Yang, T. J. Kippenberg, and K. J. Vahala, Phys. Rev. Lett. **94**, 223902 (2005).

[7] A. Schliesser, P. Del'Haye, N. Nooshi, K. J. Vahala, and T. J. Kippenberg, Phys. Rev. Lett. **97**, 243905 (2006).

[8] T. J. Kippenberg and K. J. Vahala, Opt. Express **15**, 17172-17205 (2007).

The effect on Kerr comb generation in CW-CCW mode coupled WGM microcavity

Shun Fujii(B4), Yusuke Okabe(M1), Takumi Kato(D2), Wataru Yoshiki(D2),

Akitoshi Chen-Jinnai(M2)

A WGM microcavity including a silica toroid microcavity will generate a counter propagating light as a result of defects or nanoparticles attached to its surface. We call the same direction as the input laser clockwise (CW), and the opposite direction counter-clockwise (CCW). In this work, we discuss how the interaction between the clockwise (CW) and counter-clockwise (CCW) modes affects the generation of a Kerr comb. The experimental results show a strong correlation between the mode coupling strength and the generated Kerr comb. Moreover, we performed a numerical simulation using coupled mode equations to confirm the experimental results and investigate the time domain waveform.

Keywords: Silica toroid microcavity, Four-wave mixing, Kerr comb, CW-CCW mode coupling, Coupled mode equation

1. Background

A silica toroid microcavity is an on-chip device that has an ultra high-Q and a small mode volume. Thanks to its small mode volume, the power density per unit area reaches GW/cm^2. In addition, a nonlinear process $\chi^{(3)}$ with silica will result in the generation of a Kerr comb [1]. It is known that the counter-propagating mode is induced by the reflection from impurities such as nanoparticles or material defects in whispering gallery mode (WGM) microcavities. The relationship between a microcavity and mode coupling has already been studied [2,3,4], however research on modal coupling in a Kerr comb system has just begun.[5] In this work, we demonstrate the impact of CW-CCW mode coupling on Kerr comb generation in a WGM microcavity. Because CW/CCW mode coupling is spontaneously induced by a defect, it is generally difficult to control its degree. On the other hand, when applied to a Kerr comb using a microcavity, [modal/mode?] coupling may affect the stability or accuracy of the comb. For this reason, it is very important to clarify the physics for practical Kerr comb based applications. This report summarizes work related to this matter that we undertook in 2015.

2. CW-CCW mode coupling

First, we describe the CW-CCW modal coupling in more detail. CCW light is caused by the Rayleigh scattering of CW light without a wavelength shift and shares the same path. When two modes propagating across each other are coupled, the resonance mode is split in the frequency domain. In this situation, we can define it as mode coupled. We approximate the strength of the CW-CCW mode coupling by measuring the transmittance spectrum with splitting. The splitting width increases as the coupling becomes stronger. We can determine κ and γ from the splitting and the spectrum width, and thus obtain the visibility of coupling $\Gamma = \kappa/\gamma$. In addition, because it is known that there is a high probability that CW-CCW coupling will be observed with a small diameter microcavity, we deliberately fabricated a silica toroid microcavity with a small diameter.

3. CW-CCW Kerr comb measurement

Figure 1(a) shows our experimental setup. We pumped with CW light and observed the CW and CCW directions simultaneously using an optical circulator. Figure 1(b) and (c) show the measured spectrum of the comb in the CW and CCW directions, respectively. Under adequate excitation conditions, we observed a triangular shape for the CW spectrum envelope, which is the characteristic spectrum in the soliton state. On the other hand, the spectrum in the CCW direction was not smooth. To investigate the reason for the different shape in the CCW direction, we next measured the transmission spectrum of each mode number μ as shown in Fig. 1(d). The left and right axes in Fig. 1(e) represent the peak power ratio of the CW/CCW comb components and the visibility of coupling Γ, respectively. The horizontal axis corresponds to each comb mode number μ. As a result, the Γ and the CW/CCW ratio show a strong correlation, which indicates that the CCW comb is generated by

the scattering of the CW components. The fact that CCW comb power depends on the mode coupling strength is a likely consequence, but it suggests the following things. First, the result suggests that the four wave mixing occurs in the CW direction, and that nonlinearity is not significant in the CCW direction. Next, when each Γ is not constant, the resonant peak of the superposition differs from peak to peak and the FSR is not constant. In this situation, the phase matching condition should be satisfied

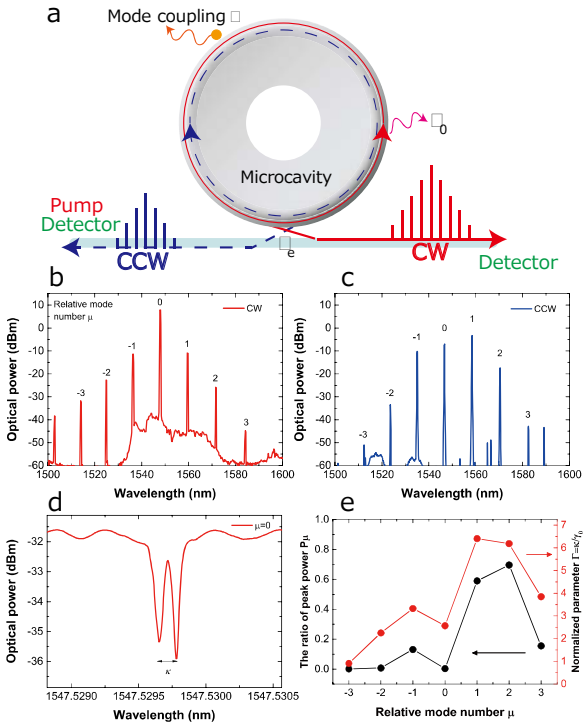

Figure 1 (a) Schematic illustration of CW and CCW combs in a microcavity. (b) Observed CW comb in the same direction as the pump and attenuated 10 dB. (c) Observed CCW comb. (d) Relationship between power ratio and coupling parameter. (e) Transmission spectrum with mode splitting.

with this cavity. Moreover, we might achieve a soliton state in the CW direction.

4. RF noise measurement

We measured the RF signal because we considered the possibility that the signals caused by mode splitting occur in the generated comb with the split modes. Previous work indicated that there is a relationship between RF noise and the temporal soliton state, and this might be serious problem in terms of the stability of the Kerr comb. Figure 2(a),(b) show the observed comb spectrum and Fig. 2(c) shows the observed RF noise signal of the CW comb in Fig. 2(a). RF signals are measured by using a photodiode and an electrical spectrum analyzer. Figure 2(d) shows the RF noise of a single comb component with the mode number μ=0,3.

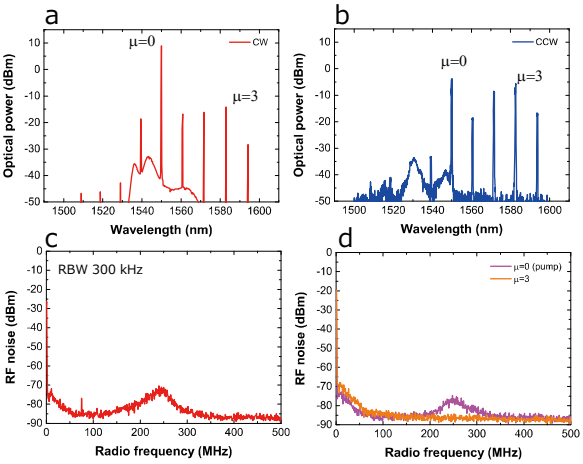

Figure 2 (a) Observed CW comb spectrum with 10 dB attenuation. (b) Observed CCW comb. (c) Measured RF signal of CW comb. (d) Solid pink and orange lines represent the RF signals of relative mode numbers μ=0 and 3, respectively.

Although the natural frequency of the cavity is detected, the signal corresponding to mode splitting did not appear. Therefore, we conclude that mode coupling has little effect on the RF region.

5. Simulation

We performed a numerical simulation of Kerr comb generation by using coupled mode equations [6]. Figure 3(a) shows a CW-CCW mode coupling model with two cavities. Since we can set the visibility of coupling Γ with respect to each mode, the ideal CW-CCW mode coupling is achieved. In this calculation, modifiable parameters are the visibility Γ, input power Pin and the cavity dispersion. We assumed that the dispersion model is a silica toroid microcavity with a major diameter of 45 μm and a minor diameter of 4 μm. Dispersion is calculated with the finite element method (FEM). Figure 3(b)-(e) show the result of the numerical simulation. Here we assume that the input power Pin is 500 mW and the mode coupling is random (Γ=1.0~5.0). As a result, even in the mode coupled condition, we could obtain a broad spectrum and a soliton waveform in the CW direction. On the other hand, there was no broad spectrum or soliton in the time domain in the CCW direction. This result corresponds to the obtained experimental result. The fact that the soliton waveform was generated is evidence that the CW comb in the experiment can be solitons. In addition, we performed the calculation on condition that the mode coupling value is constant, however, only the CW direction

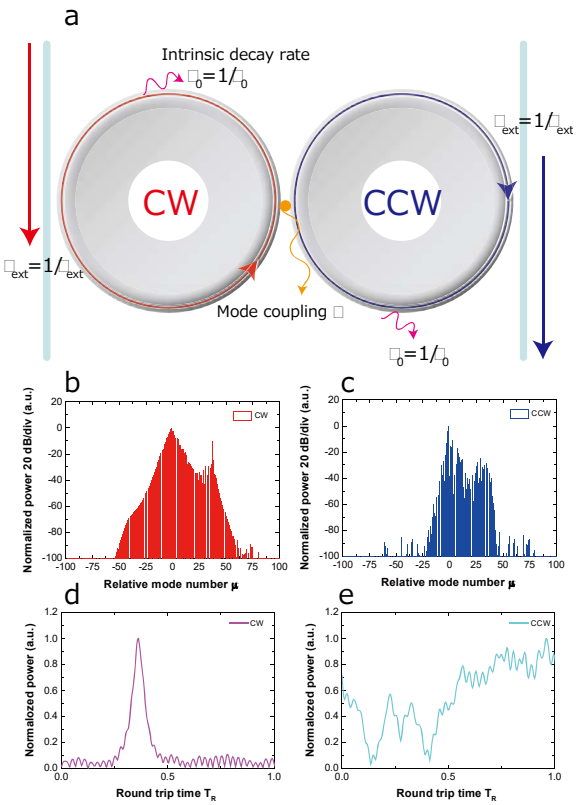

Figure 3 (a) Schematic illustration of calculation model. (b) Calculated CW comb spectrum normalized with peak power. (c) Calculated CCW comb. (d) Calculated CW waveform in time domain. This is also normalized with peak power. (e) CCW waveform corresponding to (c).

became a pulse.

6. Conclusion

We demonstrated the impact of CW-CCW coupling on Kerr comb generation in a silica toroid microcavity. Specifically, we confirmed experimentally the dependence of a CCW comb on the degree of mode coupling. In addition, there was no RF noise induced by the mode splitting. Moreover, we calculated the temporal waveform and realized soliton formation only in the CW direction, using coupled mode equations. This result reveals a definitesolution for the potential problem regarding the application of a Kerr comb with a WGM microcavity.

References

1. P. Del'haye, *et al.,* Phys. Rev. Lett. **107**, 6 (2011).
2. D. S. Weiss, *et al*, Opt. Lett. **20**, 1835-1837 (1995).
3. T. J. Kippenberg, *et al*, Opt. Lett. **27**, 1669-1671 (2002).
4. W. Yoshiki *et al.*, Opt. Express **23**, 30851 (2015).
5. Y. Liu *et al.*, Optica **1**, 137 (2014).
6. T. Hansson, *et al.*, Opt. Commun. **312**, 134-136 (2015).

Time-domain observation of strong coupling between ultra-high *Q* whispering gallery modes

Wataru Yoshiki (D2), Akitoshi Chen-Jinnai (M2), Tomohiro Tetsumoto (D1)

We report the time-domain observation of strong coupling between two coupled ultra-high *Q* whispering gallery modes. If two modes couple strongly, the light energy oscillates between them in the time domain. We employed two counter-propagating whispering gallery modes in a silica toroid microcavity for this purpose. The combination of a large coupling coefficient between the clockwise (CW) and counter-clockwise (CCW) modes and their ultra-high *Q* factor result in a clear energy oscillation in the time domain. Our measurement is based on a drop-port measurement technique, which enables us to observe the light energy in the two modes directly. The period of the energy oscillation precisely matched that inferred from the mode splitting in the frequency domain.

Key words: Silica toroid microcavity; Coupled cavity; Strong coupling; Mode splitting;

1. Introduction

Whispering gallery mode (WGM) microcavities are attractive because they typically have an ultra high *Q* and a reasonably small *V* [1]. Thanks to their high *Q*/*V* ratio, light can be strongly confined and the light-matter interaction is greatly enhanced in the cavity.

A system incorporating a coupled microcavity system is currently attracting a lot of attention. When the cavities couple strongly, it is well known that the resonance is split in the frequency domain [2]. On the other hand, photons are transferred back and forth between two cavities in the time domain, which leads to energy oscillation. Energy oscillation has already been experimentally observed and controlled in coupled photonic crystal nanocavities with the aim of achieving quantum information processing [3]. However, such experiments have yet to be reported with ultra-high *Q* WGM cavities despite the potential benefit of using an ultra high-*Q* microcavity.

In this study, we report the first time-domain observation of energy oscillation between coupled ultra-high *Q* WGMs [4]. There were two keys to achieving the observation. First, we employed two counter-propagating WGMs with a *Q* of > 10^7 in a silica toroid microcavity. It is known that the part of the light scattered by the surface couples back into a mode propagating in the opposite direction in an ultra-high *Q* WGM cavity [5]. This induces coupling between clockwise (CW) and counter-clockwise (CCW) propagating modes. By using CW and CCW modes as a platform for the experiment, we can greatly simplify the experimental setup.

In addition, we employed a drop-port measurement technique, where two tapered fibers are brought close to the cavity, to allow us to observe the energy oscillation clearly. When a single tapered fiber is employed, the light coupled into the fiber from the cavity is disturbed by interference with the light transmitted through the fiber. On the other hand, when the drop-port measurement technique is used, we can observe the light coupled from both the CW and CCW modes because there is no transmitted light in the drop-port tapered fiber.

2. Numerical analysis

First, we develop a numerical model to simulate the dynamical behavior of coupled WGMs using coupled mode theory (CMT) [6]. The master equations of the model are as follows (see Fig. 1(a));

$$\frac{da_{\mathrm{CW}}}{dt} = \left(j\omega_0 - \frac{\gamma}{2}\right) a_{\mathrm{CW}} + \frac{j\kappa}{2} a_{\mathrm{CCW}} + \sqrt{\gamma_{\mathrm{bus}}} s_{\mathrm{in}}, \quad (1)$$

$$\frac{da_{\mathrm{CCW}}}{dt} = \left(j\omega_0 - \frac{\gamma}{2}\right) a_{\mathrm{CCW}} + \frac{j\kappa}{2} a_{\mathrm{CW}}, \quad (2)$$

$$s_{\mathrm{out,t}} = s_{\mathrm{in}} - \sqrt{\gamma_{\mathrm{bus}}} a_{\mathrm{CW}}, \quad (3)$$

$$s_{\mathrm{out,r}} = \sqrt{\gamma_{\mathrm{bus}}} a_{\mathrm{CCW}}, \quad (4)$$

$$s_{\mathrm{out,dl}} = \sqrt{\gamma_{\mathrm{bus}}} a_{\mathrm{CCW}}, \quad (5)$$

$$s_{\mathrm{out,dr}} = \sqrt{\gamma_{\mathrm{bus}}} a_{\mathrm{CW}}, \quad (6)$$

where a_{CW}, a_{CCW}, s_{in}, $s_{\mathrm{out,t}}$, $s_{\mathrm{out,r}}$, $s_{\mathrm{out,dl}}$, $s_{\mathrm{out,dr}}$, ω_0, γ_{bus}, γ_{drop} and κ are the cavity mode amplitudes of the CW and CCW modes, the waveguide mode amplitudes at the input, the transmission, the reflection and the drop (left and right) ports, the angular resonant frequency, the coupling rate between the cavity and the tapered bus and drop fibers, and the coupling rate between the CW and CCW modes, respectively. If κ is larger than γ, the cavity resonance is split. Typical split cavity modes are shown in Fig. 1(b). Note that if we employ an

input signal Fourier transform that overlaps well with two peaks (dips) in Fig. 1(b), we are able to excite time-domain energy oscillation between the two modes.

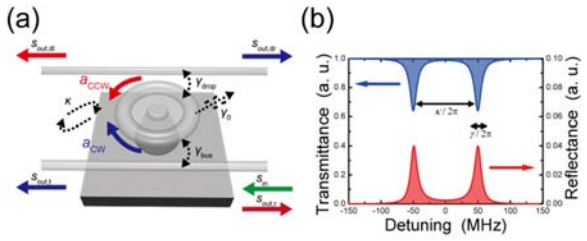

Fig 1 (a) Schematic illustration of developed model. (b) Calculated transmission (blue) and reflection (red) spectra of the cavity with (κ, γ_0, γ_{bus}, γ_{drop})/2π = (100, 10, 2.5 ,0) MHz.

Here, we discuss a method for observing energy oscillation between the CW and CCW modes. In general, we observe a transmission ($s_{out,t}$) to characterize a microcavity. However, as can be understood from Eq. (3), the transmission is the product of the interference between lights coupled from the CW mode and transmitted through a tapered fiber. So, the transmission port is not suitable for observing the energy oscillation precisely. To overcome this problem, we employ two different methods, namely 'reflection measurement' and 'drop-port measurement.' In the former method, the reflection port ($s_{out,r}$) is used. From Eq. (4), the reflection is simply proportional to the light energy in the CCW mode. On the other hand, the latter method employs an additional tapered fiber, which is called drop-port tapered fiber. The output power in a drop-port fiber is also proportional to the light energy in the cavity. A clear advantage of this method is that the energy in both the CW and CCW modes can be observed simultaneously. The reflection measurement can be performed with a single tapered fiber, which simplifies the experimental setup. This enables us to obtain data with high stability and accuracy. However, obviously it is difficult to observe the energy in CW modes with a reflection measurement. So, we first employed a reflection measurement to carefully analyze the experimental results and compare them with simulation results. Then, we confirmed that there is indeed an energy oscillation between the two modes by using a drop-port measurement.

3. Experimental results

We fabricated our silica toroid microcavity using (1) photolithography, (2) SiO_2 etching, (3) XeF_2 dry etching and (4) laser reflow [1]. We employed a tapered fiber to couple the light into the microcavity. The fabricated tapered fiber had a transmittance of over 90%. One of the transmission spectra of the fabricated microcavity is shown in the bottom panel of Fig. 2(c). There is clear resonance splitting caused by coupling between the CW and CCW modes. The linewidth of the resonance is 6.3 MHz (Q_{load} of 3×10^7) and the splitting is 85 MHz.

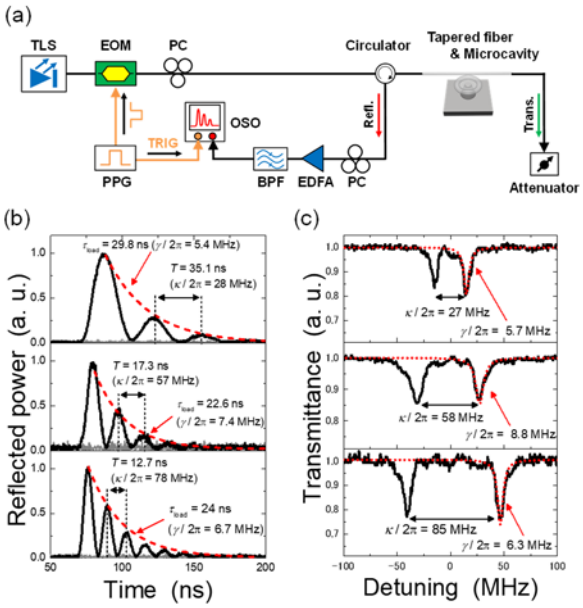

Fig. 2 (a) Experimental setup for reflection measurement. (b) Reflected signals from the cavity for different modes. Black (solid), gray (solid) and red (dashed) lines are the reflected signals with and without the cavity and the fitting curve, respectively. The input pulse widths were 10, 8 and 5 ns for the top, middle and bottom panels, respectively. It should be noted that the detected signals were offset by the remaining ASE noise and it was removed from the figure. (c) The transmission spectra of the modes employed in (b).

First, we performed a reflection measurement. Figure 2(a) is a block diagram of the experimental setup. The continuous light output from a tunable laser source (TLS) is turned into rectangular pulses using an electro-optical modulator (EOM). The RF signal driving the EOM is generated by a pulse pattern generator (PPG). The trigger signal is input into an optical sampling oscilloscope (OSO). A polarization controller (PC) is employed to adjust the polarization of the input light. An optical circulator is used to extract reflected light. The reflected light from a microcavity is amplified with an erbium-doped fiber amplifier (EDFA). Finally, the OSO detects and records the reflected light. Figure 2(b) shows the reflected signal from the cavity for different modes (different cavities). As can be seen, the reflected signal oscillates periodically when we input a signal with a rectangular shape. This suggests that there is an energy oscillation between the CW and CCW modes although only a CCW mode (a reflected signal) can be observed with this setup. The oscillation period in each panel is different due to the difference in the coupling rate κ. Figure 2(c) shows transmission

spectra that correspond to Fig. 2(b). γ and κ that can be estimated from the spectra shown in Fig. 2(c) agree well with those calculated from the reflected signals shown in Fig. 2(b). This agreement also suggests that the oscillation in the reflected signal is due to the coupling between the CW and CCW modes.

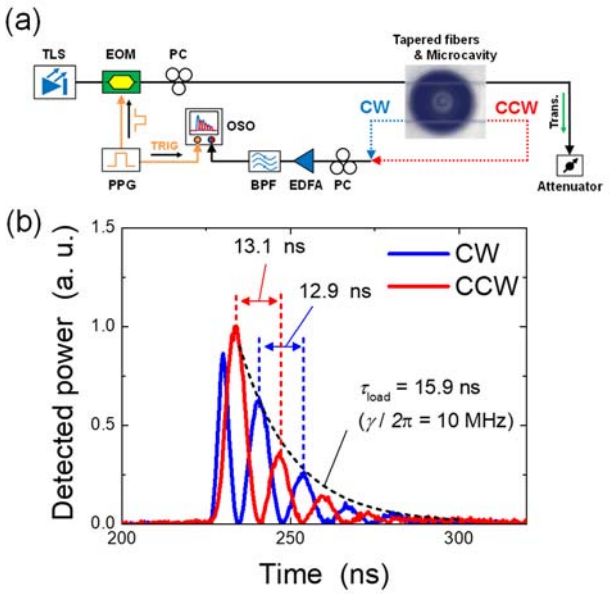

Fig. 3 (a) Experimental setup for drop-port measurement. (b) Output power measured at the drop port. The blue and red solid lines represent the output from the CW and CCW modes, respectively. Note that the timings of the two signals were calibrated by measuring the delays between the two signals.

Finally, we describe experiments based on the drop-port measurement. By using this method, we confirmed that there is indeed an energy oscillation between the two modes. The experimental setup is shown in Fig. 3(a). The energies in the CW and CCW modes are extracted directly from the drop-port tapered fiber, and are then detected with the OSO after amplification. Note that our drop-port tapered fiber is bent and its position is manipulated independently by a nanopositioner. This setup enables us to control the coupling rate between the drop-port tapered fiber and the cavity easily and accurately. Despite being bent, the fabricated tapered fiber has a transmittance of over 80%. Figure 3(b) shows the result of the drop-port measurement. We employed the same modes as in the bottom panel of Figs. 2(b) and 2(c). As seen from the figure, the energy clearly oscillates between the CW and CCW modes. This is direct evidence showing that there is indeed an energy oscillation between the CW and CCW modes. In addition, the oscillation period agrees well with that estimated in Fig. 2(b). Here γ is slightly larger than that in Fig. 2(b). This is believed to be due to the additional coupling loss induced by the drop tapered fiber. From the figure, we can conclude that we observed the energy oscillation between counter propagating WGMs. This is the first observation of coupling between modes with an ultra high Q of over [107/10⁷?] in the time domain.

4. Conclusion

In conclusion, we have reported the first observation of energy oscillation between two coupled ultra-high *Q* whispering gallery modes in the time domain. We employed CW and CCW modes in a silica toroid microcavity because they provided a good platform for our experiments. Thanks to the large Γ, which is due to the large coupling rate between the two modes and an ultra-high *Q* factor, clear energy oscillation was excited and observed. By using the reflection measurement, we confirmed that the oscillation periods in the time domain were the same as those inferred from the mode splitting in the frequency domain. In addition, we observed the energy oscillation between the CW and CCW modes simultaneously by taking advantage of the drop-port measurement technique. We believe that our results pave the way toward the development of a method for controlling the coupling states between ultra high *Q* microcavities, which is important in terms of achieving quantum information processing.

References

[1] D. Armani, T. Kippenberg, S. Spillane, and K. Vahala, "Ultra-high-*Q* toroid microcavity on a chip," Nature **421**, 925–928 (2003).

[2] C. Zheng, X. Jiang, S. Hua, L. Chang, G. Li, H. Fan, and M. Xiao, "Controllable optical analog to electromagnetically induced transparency in coupled high-*Q* microtoroid cavities," Opt. Express **20**, 18319-18325 (2012).

[3] Y. Sato, Y. Tanaka, J. Upham, Y. Takahashi, T. Asano, and S. Noda, "Strong coupling between distant photonic nanocavities and its dynamic control," Nat. Photonics **6**, 56–61 (2012).

[4] W. Yoshiki, A. Chen-Jinnai, T. Tetsumoto and T. Tanabe, "Observation of energy oscillation between strongly-coupled counter-propagating ultra-high *Q* whispering gallery modes," Opt. Express **23**, 30851-30860 (2015).

[5] T. Kippenberg, S. Spillane, and K. Vahala, "Modal coupling in traveling-wave resonators," Opt. Lett. **27**,1669–1671 (2002).

[6] W. Yoshiki and T. Tanabe, "Analysis of bistable memory in silica toroid microcavity," J. Opt. Soc. Am. B **29**, 3335–3343 (2012).

Dispersion tailoring of a crystalline WGM microcavity for an octave-spanning optical frequency comb

Yosuke Nakagawa (M2)

Whispering gallery mode (WGM) microcavities have been intensively studied as a platform for generating optical frequency combs. To generate an optical frequency comb, an octave-spanning optical Kerr frequency comb is needed to perform the f-2f self-referencing method. Several numerical studies have already been reported on the use of dispersion tailoring to achieve an octave-spanning optical Kerr frequency comb. In this report, we tailored the dispersion by controlling the microcavity shape using a fabrication process involving ultra-precise cutting. And we demonstrated optical Kerr comb generation by using tailored dispersion in a simulation.

Key words: Whispering-gallery-mode microcavity, CaF_2, Optical Kerr comb, dispersion

1. Introduction

A microcavity with an ultra-high quality factor (Q) and a small mode volume (V) is suitable for applications requiring a nonlinear optical effect. An optical Kerr comb is generated by employing cascaded four wave mixing (FWM) in the microcavity. Then, the Q-factor is calculated with the following equation.

$$Q_{total} = \left(Q_{scat}^{-1} + Q_{abs}^{-1} + Q_{coup}^{-1} + Q_{etc}^{-1}\right)^{-1} \quad (1)$$

Where Q_{scat}, Q_{abs} and Q_{coup} are obtained from the surface scattering loss, material absorption loss and coupling loss of the waveguide. Q_{scat} and Q_{coup} can vary depending on the fabrication and experiment. Thus in theory the highest Q-factor depends on Q_{abs}. Figure 1 shows Q_{abs}, and CaF_2 has the highest Q_{abs} value [1]. The CaF_2 microcavity has the highest experimental Q-factor of 6.3×10^{10} [2]. Therefore, we fabricated a CaF_2 microcavity and tried using it to generate an optical frequency comb.

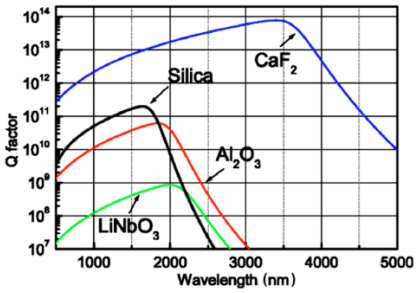

Fig. 1 Projected limitation of Q factor for WGM microcavity by bulk material attenuation [1].

2. Stabilization of optical Kerr comb

An optical frequency comb has a strictly equidistant and very broad spectrum that consists of equidistant lines similar to a comb in the frequency domain. The frequency of the optical frequency comb is calculated with the following equation.

$$f(n) = nf_r + f_o \quad (2)$$

Where f_r and f_o are the repetition and offset frequencies, respectively. To generate an optical frequency comb, we need to measure these two values. The offset frequency is measured by using the f-2f interference [3]. The f-2f interference method needs the optical Kerr frequency comb over one octave, and the offset frequency is calculated with the following equation.

$$\begin{aligned} 2f(n) - f(2n) &= 2(nf_r + f_o) - (2nf_r + f_o) \\ &= f_o \end{aligned} \quad (3)$$

The optical Kerr frequency comb is not generated over one octave in a microcavity, thus f-2f interference is not realized. Therefore, broadening the wavelength range of an optical Kerr comb by tailoring the dispersion has been studied [4, 5].

3. Dispersion of microcavity

The free spectral range (FSR) is the optical frequency spacing between two adjacent modes, and is calculated with the following equation.

$$\nu_{FSR} = \frac{c}{2\pi n(\omega)R} \quad (4)$$

Here c, n, ω and R are the velocity of light, refractive index, angular frequency and the radius of the microcavity, respectively. The FSR depends on the refractive index and so is not constant. Therefore, as shown in Fig. 2, an optical Kerr frequency comb in a microcavity is not spread over one octave.

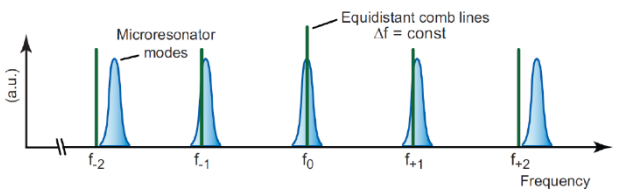

Fig. 2 Frequency comb generation in a dispersive resonator. The mismatch between equidistant frequency comb lines

and the non-equidistant resonator modes hinders broadband frequency comb generation in a microcavity [6].

The dependence of the propagation constant on angular frequency is calculated with the following equation.

$$\beta(\omega) = \beta_0 + \beta_1 \cdot (\omega - \omega_0) + \frac{1}{2}\beta_2 \cdot (\omega - \omega_0)^2 + \sum_{m=3}^{m} \frac{1}{m!}\beta_m \cdot (\omega - \omega_0)^m \quad (5)$$

Here, β_1 and β_2 are group delay time and group velocity dispersion, respectively. The total dispersion is calculated from the geometrical dispersion and material dispersion and is almost equal to their sum. Material dispersion cannot be controlled and is calculated with the following equation.

$$\beta_2 = -\frac{\lambda^2}{2\pi c^2} \cdot \frac{d^2 n}{d\lambda^2} \quad (6)$$

Figure 3 shows the CaF_2 material dispersion.

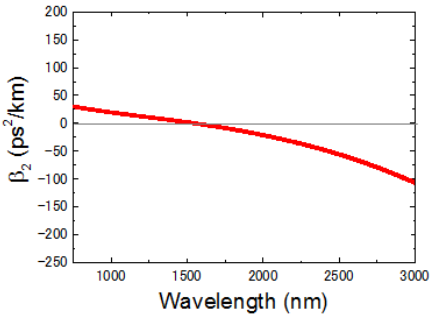

Fig. 3 Material dispersion of CaF_2.

Light is confined in the microcavity. However, as shown in Fig. 4, the microcavity leaks a little light. Thus the effective refractive index is calculated with the following equation.

$$n_{eff} = \frac{n_{material} \cdot \iint_{material} E \cdot E^* + n_{air} \cdot \iint_{air} E \cdot E^*}{\iint_{all} E \cdot E^*} \quad (7)$$

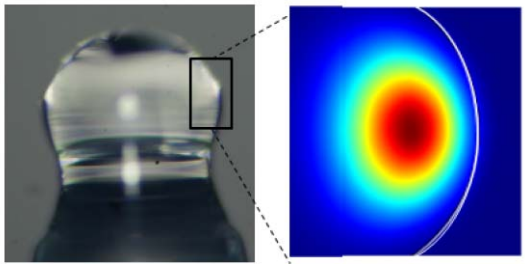

Fig. 4 Sapphire microcavity (left). Cross-section of electrical field distribution (right)

Geometrical dispersion cannot be calculated using the effective refractive index because the radius of a microcavity depends on the wavelength. Thus a geometrical microcavity is calculated with the following equation.

$$\beta_2 = -\frac{1}{4\pi^2 R} \cdot \frac{\Delta(\Delta\nu_l)}{(\Delta\nu_l)^3} \quad (8)$$

4. Tailoring dispersion

Since the Kerr effect modulates the pulse in the direction of normal dispersion, a structure with an anomalous dispersion is needed to generate a Kerr comb to balance the dispersion. So, the first step is to find a structure that exhibits an anomalous dispersion over one octave. The total dispersion is calculated from the geometrical dispersion and material dispersion and is almost equal to their sum. Therefore, we tailor the geometrical dispersion of the microcavity by designing the cross-section of the microcavity shape because the material dispersion cannot be controlled. We designed some structures and performed a calculation using COMSOL. Figures 5, 6 and 7 show the dispersions for microcavities with triangular, rectangular and trapezoidal cross-sections.

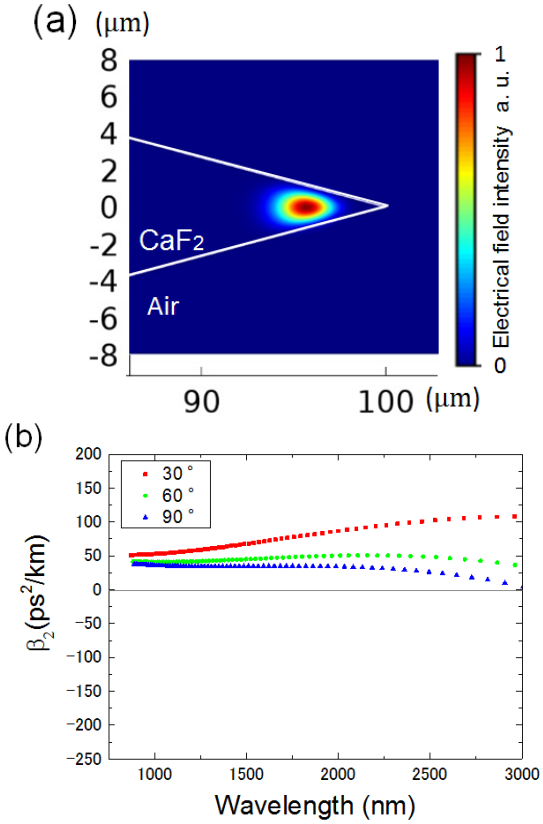

Fig. 5 (a) Electrical field intensity profile of WGM microcavity with triangular cross-section whose angle is 30 ° and TE polarization. The mode volume of this microcavity is 2234 μm^3. (b) Calculated dispersions for (a) with triangular angles of 30, 60 and 90° .

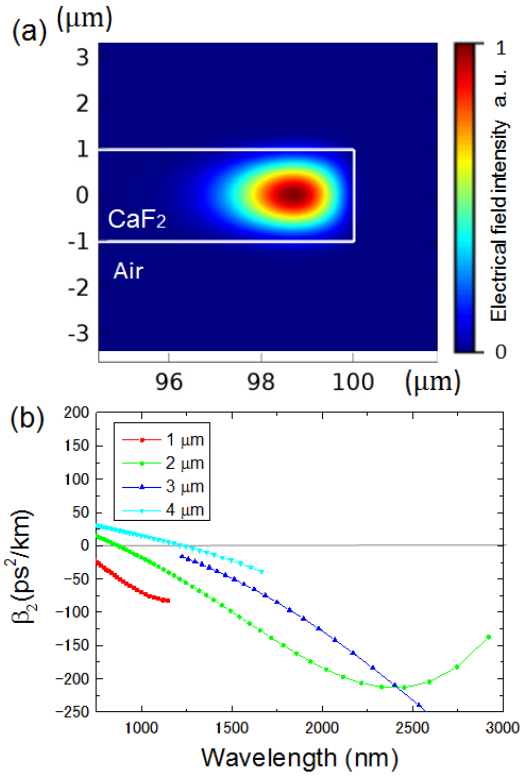

Fig. 6 (a) Electrical field intensity profile of WGM microcavity with rectangular cross-section whose width is 2 μm and TE polarization. The mode volume of this microcavity is 1535μm^3. (b) Calculated dispersions for (a) with rectangular widths of 1, 2, 3 and 4 μm.

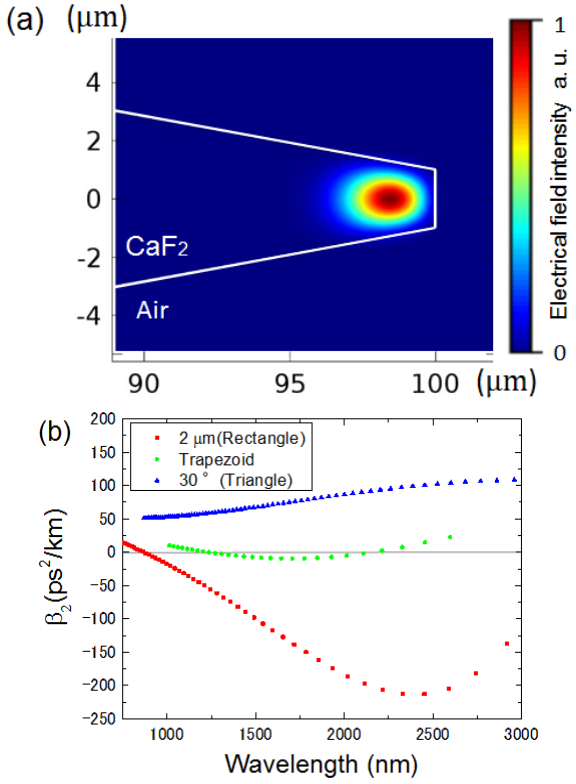

Fig. 7 (a) Electrical field intensity profile of WGM microcavity with trapezoidal cross-section and TE polarization. The mode volume of this microcavity is 2154μm^3. (b) Calculated dispersions for (a), triangular (30°) and rectangular (2 μm) cross-sections.

The radii of the microcavities shown in Figs. 5, 6 and 7 are 100 μm. As shown Fig. 5(b), the triangular shape has angular dependence. As the triangular angle increases, the dispersion becomes low and have a normal value. And as shown in Fig. 6(b), the rectangular shape also has width dependence. As the rectangular width increases, the dispersion shifts to a longer wavelength. Although overall the rectangular shape shows an anomalous dispersion, the value rises steeply at longer wavelengths. On the other hand, the dispersion for a triangular shape rises gently in the same wavelength regime. Therefore, we combine these two effects. Figure 7(b) shows the dispersion for a microcavity with a trapezoidal cross-section. As shown Fig. 7(b), the trapezoidal shape microcavity has a low anomalous dispersion, therefore we tried to fabricate a microcavity with a trapezoidal shape. However, we were unsuccessful because of the fragility of CaF_2.

Therefore, we considered other trapezoidal structures that can be fabricated. Figure 8 shows the microcavity we designed, which has a low anomalous dispersion. The two zero dispersion wavelengths are located at 1313 nm and 2771 nm and are separated by one octave. The dispersion value ranges from 0 to -46 ps^2/km. The width of the trapezoidal upper and lower lines are 5 and 6 μm, respectively. The height of the trapezoid is 6 μm. The radius of the microcavity is 262 μm and the mode volume is $1.27 \times 10^4\ \mu m^3$. Consequently, we were able to design a microcavity with a low anomalous dispersion over one octave.

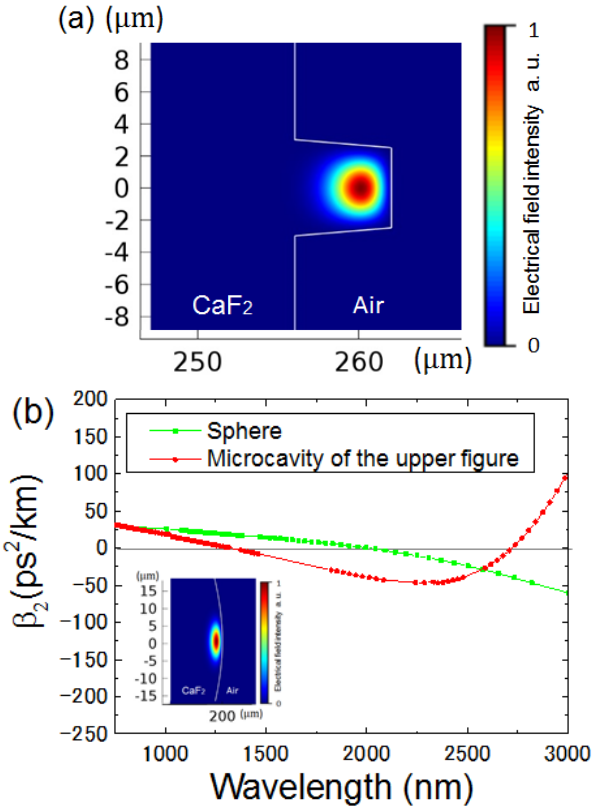

Fig. 8 (a) Electrical field intensity profile of WGM microcavity with trapezoidal cross-section and TE polarization. (b) Calculated dispersions for (a) and spherical microcavity with a 200 μm radius as shown in the inset.

5. Optical Kerr comb simulation

To demonstrate the role of the designed dispersion numerically, we performed an optical Kerr frequency comb simulation. Our simulation is based on a split-step Fourier method, which is modeled by the following equation.

$$t_R \frac{\partial E}{\partial \tau} = \left[-\frac{\alpha}{2} - \frac{\kappa}{2} - i\delta_0 + iL \sum_{k\geq 2} \frac{\beta_k}{k!} \left(i\frac{\partial}{\partial t} \right)^k + i\gamma L |E|^2 \right] E + \sqrt{\kappa} S \quad (3)$$

Where t_R, α, κ, δ_0, L, β, γ, and S are the round-trip time, intrinsic cavity loss, coupling loss, detuning of the input wavelength, cavity length, dispersion of the microcavity, nonlinear coefficient, and input power, respectively. The intrinsic cavity loss and coupling loss correspond to Qint and Qcouple, respectively. Also, the γ value is 9.96 × 10^{-8} $W^{-1}m^{-1}$ calculated from the mode volume. The designed microcavity can be fabricated by using an ultra-precise cutting process. Since the *Q*-factor is strongly limited by surface roughness, a *Q* of under 1.2×10^6 is feasible. Hence, we calculated the condition $Q_{int} = Q_{coup} = 2.4 \times 10^6$. Then α and κ are 1.68×10^{-6} μm^{-1}. And we used the tailored dispersion shown in Fig. 8(b). L and δ_0 are 2346 μm and 0.2 μm, respectively. In this work, considering the red shift derived from the Kerr effect, we scan the pump wavelength from a resonant wavelength to a longer wavelength. The scan speed is 0.4 μm/s. The input power is 3 W. Figure 9(a) and (b), respectively, show the intra-cavity comb spectrum and the temporal waveform when the pump wavelength is detuned from a resonant wavelength to a longer wavelength.

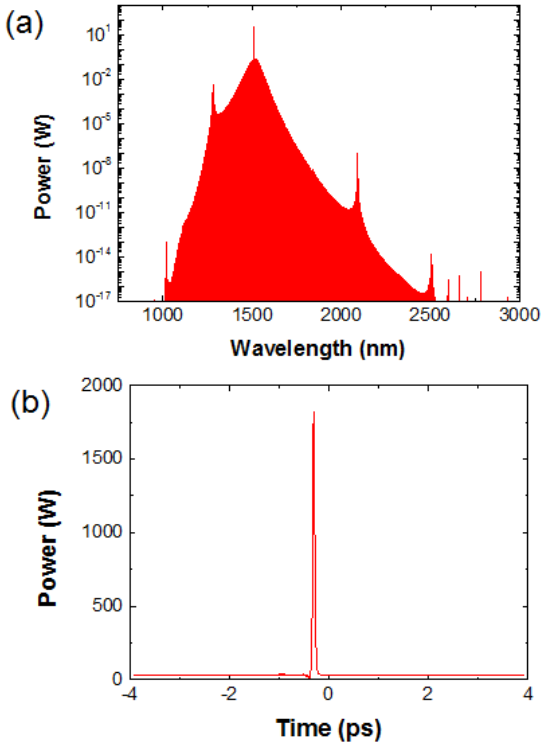

Fig. 9 (a) Intra-cavity power in simulation. Input power is 3 W and scan speed is 0.4 μm/s. Optical Kerr frequency combs are generated over one octave by using the tailored dispersion shown in Fig. 8(b). (b) Temporal waveform per round trip.

As shown by the result in Fig. 9(a), the range of the wavelength spread over one octave from 1100 to 2200 nm. Thanks to the octave-spanning optical Kerr frequency comb, a short 60 fs pulse with a peak power of 1827 W is obtained as shown in Fig. 9(b).

6. Fabrication and measurement of designed microcavity

Figure 10 shows the designed CaF_2 microcavity that we fabricated with a cutting machine.

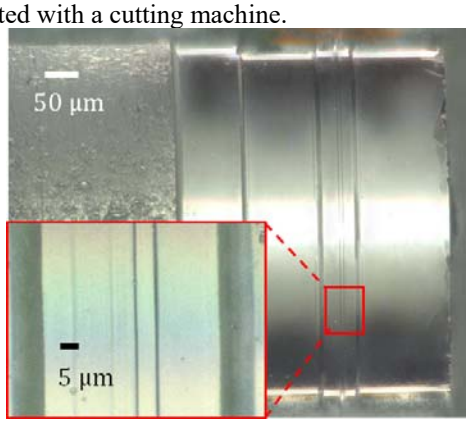

Fig. 10 Microscope image of CaF_2 microcavity. The radius is 262 μm. This microcavity was fabricated using an ultra-precise computer controlled lathe. The inset shows the resonance point of the microcavity.

We measured the surface of the microcavity using a Scanning White Light Interferometer (ZYGO) as shown in Fig. 11.

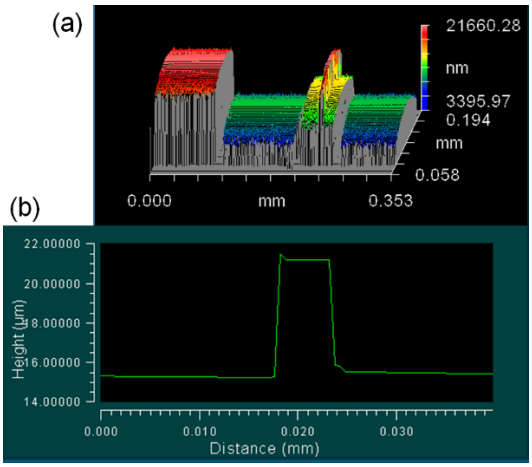

Fig. 11 (a) ZYGO image of microcavity surface. (b) ZYGO image of microcavity cross-section.

As shown in Figs. 10 and 11, we were able to fabricate the CaF_2 microcavity according to the design. We measured the transmittance spectrum of this microcavity to measure the *Q*-factor with a setup using a tapered fiber. Figure 12(a) shows the spectrum, and we obtained a Q of 1.2×10^6. Figure 12(b) and (c) show the experimental result of the dispersion measurement. However, the laser changes wavelength between 1480 and 1640 nm, so we measured

only a narrow range as shown in Fig. 12(b). As also shown in Fig. 12(b), the dispersion value is low and anomalous and corresponds well with the simulation result.

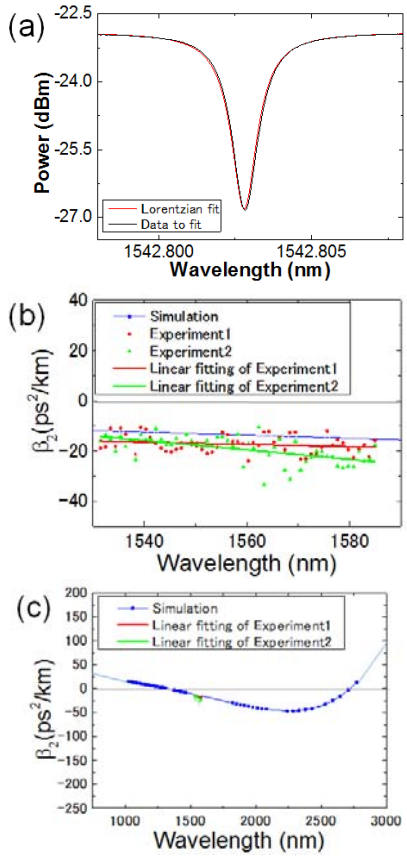

Fig. 12(a) Transmission spectrum of the microcavity shown in Fig. 10 measured with a conventional tapered fiber setup. The Q factor is 1.2×10^6 (b) (c) Calculated and measured dispersion of microcavity shown in Fig. 10.

7. Conclusion

We designed a CaF_2 WGM microcavity with an anomalous dispersion range over one octave between 1313 and 2771 nm. In addition, we used a numerical simulation to demonstrate that octave spanning optical Kerr frequency combs could be generated in our designed microcavity. And we fabricated the designed microcavity using only an ultra-precise computer controlled lathe and measured the anomalous dispersion, which agreed well with the simulation value. We were able to fabricate a microcavity which is designed to have an anomalous dispersion over one octave. This achievement will pave the way to the microminiaturization of the conventional optical frequency comb source.

References

[1] A. A. Savchenkov, V. S. Ilchenko, A. B. Matsko, and L. Maleki, Phys. Rev. A **70**, 051804(R) (2004).
[2] I. S. Grudinin, A. B. Matsko, A. A. Savchenkov, D. Strekalov, V. S. Ilchenko, L. Maleki, Optics Communications 265, 33–38, (2006).
[3] H. R. Telle, G. Steinmeyer, A. E. Dunlop, J. Stenger, D. H. Sutter, and U. Keller, Appl. Phys. B 69, 327 (1999).
[4] I. S. Grudinin, and N. Yu, Optica, 2, 221 (2015).
[5] L. Zhang, C. Bao, V. Singh, J. Mu, C. Yang, A. M. Agarwal, L. C. Kimerling, and J. Michel, Opt. Lett. 38 5122 (2013).
[6] P. Del'Haye, PhD thesis, (2011).

Nonlinear optical effects in silica-gold composite toroidal microcavity

Sho Tamaki (M2)

In this study, we describe numerically the enhancement of nonlinear optical effects in silica-gold composite material, methods for fabricating silica-gold composite toroidal microcavities and their basic optical properties.

Key words: Gold nanoparticle, Silica toroidal microcavity and Localized surface plasmon resonance

1. Introduction

Optical microcavities are being closely studied for future telecommunication devices. The ideal properties of an optical microcavity are a high quality factor (Q) and high third-order nonlinear susceptibility. Among the many different types of optical microcavities, the silica toroidal microcavity is widely renowned for its high Q and its capacity for fabrication on a Si-chip. However, due to the material property of silica, its third-order nonlinear susceptibility $\chi^{(3)}$ is relatively small. On the other hand, the localized surface plasmon resonance in metal nanoparticles exhibits large third-order nonlinear susceptibility and a small Q due to light absorption. Using these facts as a basis, this study aimed to obtain a high Q and large third-order optical nonlinearity by combining localized surface plasmon resonance and a silica toroidal microcavity.

2. Numerical study of nonlinear optical effects in silica-gold composite material

2.1 Numerical analysis

We can expect to enhance $\chi^{(3)}$ and decrease the Q factor by doping a silica toroidal microcavity with gold. Therefore, we investigated which effect is more dominant as a total nonlinear optical effect in the cavity. As an indicator of the total nonlinear optical effect in the cavity, we used $Q \times \chi^{(3)}$, since the intra-cavity energy [1] is given as

$$U_{switch} = \frac{\varepsilon_0 \varepsilon n_0^2 V_{cavity}}{2 n_2 Q} \qquad (1)$$

Note that n_2 is proportional to $\chi^{(3)}$. ($n_2 \propto \chi^{(3)}$)

We used the following process to calculate the indicator.

1. Calculate the complex dielectric constant of a gold nanoparticle.
2. Calculate the complex dielectric constant of silica-gold composite material.[2]
3. Calculate the material Q factor and $\chi^{(3)}$.
4. Calculate the fraction volume dependence of the product of the minimum Q factor and the maximum $\chi^{(3)}$.

The final result for the indicator is given in Fig. 1.

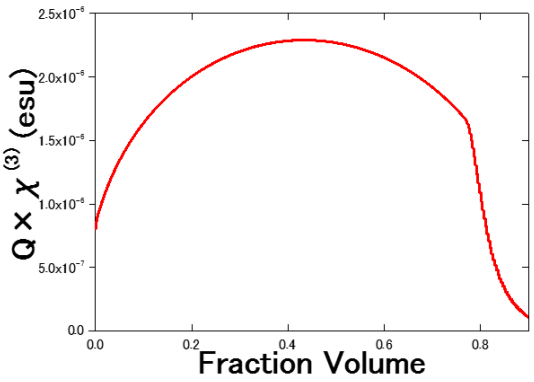

Fig. 1: Fraction volume versus $Q \times \chi^{(3)}$ for gold NP diameter of 100 nm.

2.2 Discussion

In Fig. 1, it can be inferred that $Q \times \chi^{(3)}$ shows its optimum value when the fraction volume is around 0.4. However, it should be noted that this calculation assumes a situation where all the gold particles are spherical and completely dispersed in the medium. Therefore, as the fraction volume increases, the calculation accuracy deteriorates.

3. Fabrication and optical properties

3.1 Fabrication

We adopted the sputtering and sol-gel methods to fabricate a silica-gold composite toroidal microcavity. Figures 2 and 3 outline the schemes we used for the sputtering and sol-gel methods,

respectively.

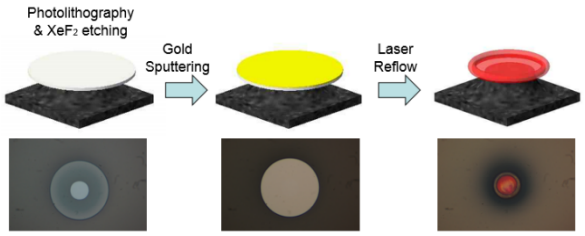

Fig. 2: Fabrication of silica-gold composite microcavity

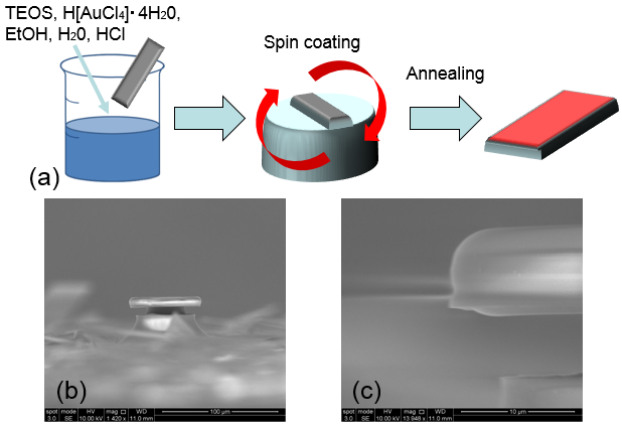

Fig. 3(a): Schematic of sol-gel method. (b) and (c): SEM images of cavity fabricated by sol-gel method.

3.2 Optical properties

We measured the Q factors of the fabricated cavities using the experimental set up shown below. We scanned the cavity resonance wavelength using the thermo-optic effect since the laser wavelength (520 nm) was fixed to the localized surface plasmon resonance wavelength.

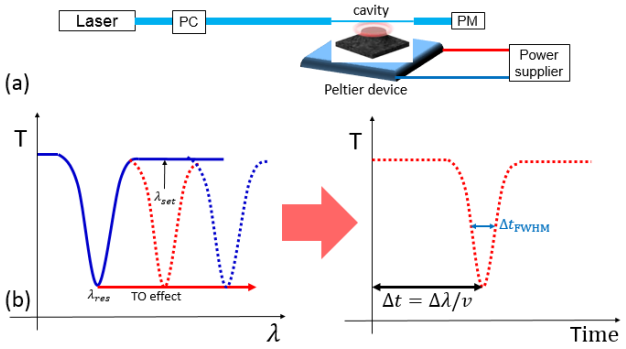

Fig. 4(a): Experimental setup. (b): Q factor measurement using TO effect.

With this set up, we measured the Q factors at the telecommunication wavelength and the localized surface plasmon resonance wavelength with different fraction volumes. Figure 5 shows the summarized experimental results for the Q factors and the theoretical Q factors.

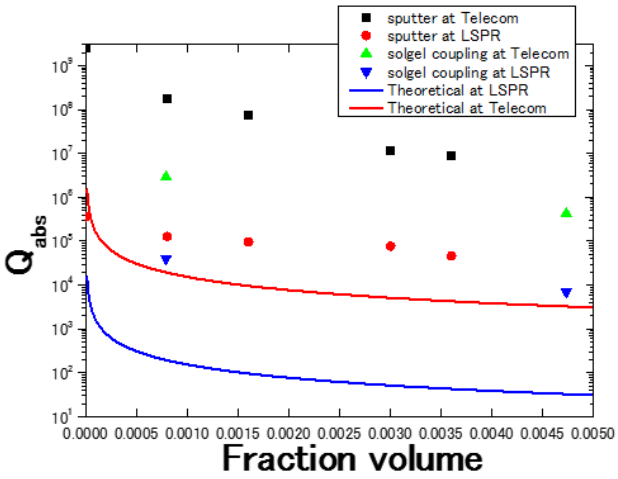

Fig. 5: Summarized experimental results for Q factor.

3.2 Discussion

As can be inferred from Fig. 5, the Q factors of cavities fabricated with the sol-gel method are closer to the theoretical values than those obtained with the sputtering method. This is because, with the sputtering method, the gold nanoparticles are heated above their melting point with a laser reflow process, whereas the sol-gel method is performed below the melting point. Therefore, with the sol-gel method there is much less chance of the aggregation of gold nanoparticles, and the optical properties are superior to those obtained with the sputtering method.

4. Conclusion

To summarize this study, we demonstrated the enhancement of nonlinear optical effects numerically and fabricated silica-gold composite toroidal microcavities with the sputtering and sol-gel methods. Using the thermo-optic effect, we succeeded in measuring the Q factors of the fabricated cavities and showed that the sol-gel method produces superior optical properties to those obtained with the sputtering method.

References

[1] M. Notomi, A. Shinya, K. Nozaki, T. Tanabe, S. Matsuo, E. Kuramochi, T. Sato, H. Taniyama, and H. Sumikura, "Low-power nanophotonic devices based on photonic crystals towards dense photonic network on chip," IET Circuits Devices Syst. **5**, 84–93 (2011).

[2] D. Compton, L. Cornis, and E. van der Lingen, "The third order nonlinear optical properties of gold nanoparticles in glasses part 1," Gold Bulletin. **36**, 10-16 (2003).

Fabrication of erbium-doped silica toroid microcavity and theoretical consideration for lasing

Atsuhiro Hori(B4)

We fabricated an erbium-doped silica toroid microcavity using ion implantation and evaluated its characteristics by optical measurement. We also calculated the threshold condition for lasing and developed a re-design proposal as regards quality factor and erbium concentration.

Key word : erbium-doped silica toroid microcavity, Lasing, Coupling mode theory, Rate equation

1. Introduction

An optical microcavity is a device that can confine light and store it in a very small space for a long time. The silica toroid microcavity, which is a whispering gallery mode cavity, has a high quality factor and a small mode volume and is suitable for integration. Rare earth elements have very useful properties for optical devices. In particular, erbium exhibits photoluminescence around 1550 nm, which is the wavelength used in telecommunication. Therefore, erbium is used in fiber amplifiers (EDFA) and fiber lasers.

The combination of a silica toroid microcavity and erbium can create new applications. In fact, erbium-doped silica toroid microcavities are used in sensing [1], add-drop filters [2], and parity-time symmetry [3].

In this research, we aimed at lasing and fabricated an erbium-doped silica toroid microcavity using ion implantation as a first step towards application. Moreover, we considered the lasing threshold condition theoretically using coupling mode theory and a rate equation.

2. Lasing threshold condition

To calculate the lasing threshold condition, we used an equation of motion for the lasing mode and a rate equation for the erbium laser system [4].

$$\frac{da_s}{dt} = -\frac{1}{2\tau_s}a_s + g_s a_s \qquad (1)$$

$$\frac{dN_2}{dt} = W_{12}N_1 - W_{21}N_2 - \frac{N_2}{T} \qquad (2)$$

Where a_s is the internal cavity field at the lasing wavelength, τ_s is the cavity photon lifetime, g_s is the intracavity gain coefficient depending on the mode, N_1, N_2 is the ground state (or excited state) population, W_{12}, W_{21} is the absorption (or stimulated emission) transition rate, and T is a spontaneous emission lifetime. g_s is determined by N_1, N_2. The lasing threshold condition is given by setting the first equation at zero (i.e., when the gain compensates for the total cavity losses).

Figure 1 shows the lasing threshold condition calculated by substituting a typical value for W_{12}, W_{21}, T. For example, $Q_0 = 1 \times 10^7$ and when the erbium concentration is about 2.8×10^{18} cm^{-3}, lasing can be obtained.

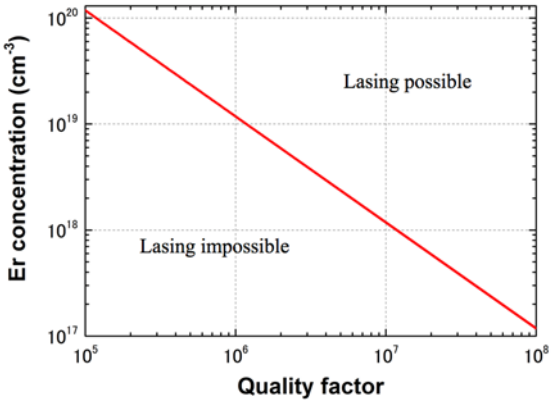

Fig. 1: Lasing threshold condition as a function of intrinsic quality factor and erbium concentration.

3. Fabrication

First, erbium ions are implanted in a SiO_2-Si substrate (SiO_2 thickness is 1 μm). The subsequent processes are the same as those used for an undoped silica toroid microcavity. All the samples are implanted with 194 keV at a fluence of 7×10^{14} cm^{-2}. When SiO_2 is wet-etched in HF, the outer perimeters of the microdisks are undercut and the implanted erbium ions disappear. We assume that this undercut is because ion implantation made the SiO_2 structure fragile. To prevent this, we dry-etched the SiO_2 in CHF_3, then the microdisks warped but there was no undercut. These warped microdisks were transformed into well-sharped toroid microcavities by CO_2 laser reflow.

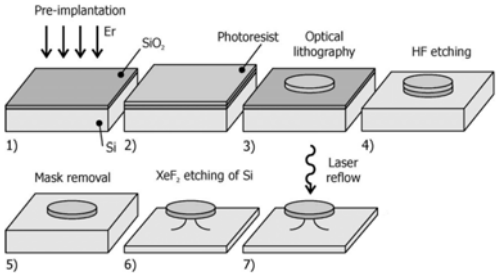

Fig. 2: Processes for fabricating erbium-doped silica toroid microcavities. [J. Kalkman, *et al.*, J. Appl. Phys. **99**, 1-9 (2006)]

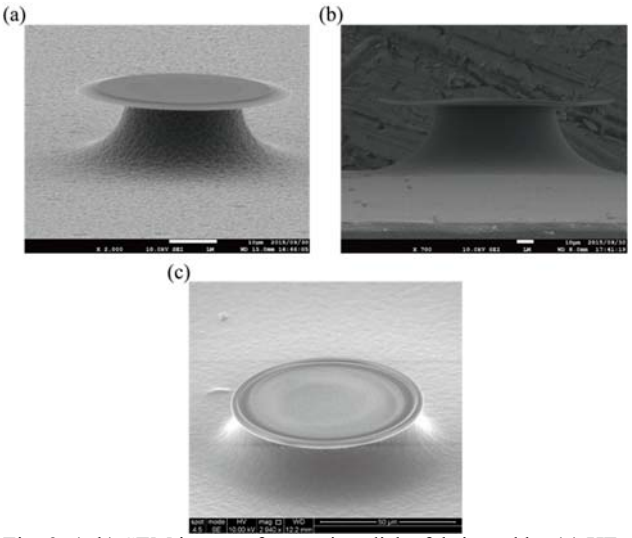

Fig. 3: (a,b) SEM image of two microdisks fabricated by (a) HF wet etching (b) CHF_3 dry etching. (c) SEM image of erbium-doped silica toroid microcavity.

4. Evaluation of characteristics

An intrinsic Q of 3.58×10^5 was derived from the measured transmittance spectrum of a fabricated microcavity. From Fig. 1, the erbium concentration required for lasing with this intrinsic Q is 1.0×10^{20} cm^{-3}. Assuming that the erbium ions were diffused homogeneously by the laser reflow, a fluence of 7×10^{14} cm^{-2} corresponds to a concentration of 7×10^{18} cm^{-3} and cannot reach the lasing threshold condition. In fact, despite pumping at 1480 nm lasing was not obtained.

To evaluate the microcavity characteristics, we measured the variation in quality factor caused by pumping. When pumped at 1481 nm, the measured quality factors varied slightly from $Q_{tot} = 1.13 \times 10^5$ to $Q_{tot} = 1.18 \times 10^5$, and similar results were obtained multiple times. We assume that the slight increase in quality factor is due to the gain of the pumped erbium ions.

To consider this result, we introduce the quality factor dependence on erbium gain.

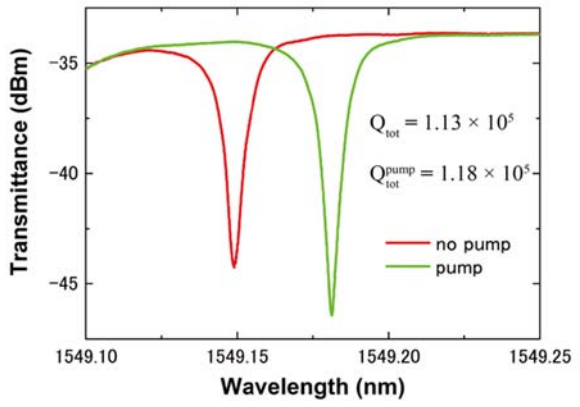

Fig. 3: Transmittance spectrum pumped at $\lambda = 1481$ nm .

$$\frac{1}{Q^{Er}} = \frac{\lambda}{2\pi n}\left[-\frac{N_2}{N_T}(\alpha + g^*) + \alpha\right] \quad (3)$$

$$\frac{1}{Q_{tot}} = \frac{1}{Q_0} + \frac{1}{Q_e} + \frac{1}{Q^{Er}} \quad (4)$$

Where, λ is the resonance wavelength, and $N_T = N_1 + N_2$. α, g^* were defined as $\alpha = N_T\sigma^a$, $g^* = N_T\sigma^e$. In these expressions σ^a, σ^e were the absorption/emission cross-sections of erbium ions at the resonance wavelength. From these equations, pumping with the theoretical quality factor $Q_{tot} = 1.20 \times 10^5$ was calculated, which agreed well with the experimental value.

5. Re-design proposal

In this research, the main reason for no lasing is that the cavity quality factor is too low. By improving the fabrication processes, we will obtain $Q_0 = 1 \times 10^7$, namely the value that an undoped silica toroid microcavity generally obtains. We used substrates with a 1 μm SiO_2 thickness but thin silica disks tend to warp and silica toroids are also the same after laser reflow. The heat of the dry etching processes denatures the photoresist and it becomes hard to remove. The remaining photoresist reduces the quality factor. Moreover, because ion implantation damages the silica structure, the implantation process is often followed by thermal annealing but in this research we substituted laser reflow for thermal annealing. On the basis of the above, we considered improvements in the fabrication processes that use substrates with 2 μm SiO_2 thickness, careful removal of the photoresist by O_2 ashing, and performing thermal annealing after ion implantation.

With regard to the erbium concentration, when $Q_0 = 1 \times 10^7$ is obtained, an erbium concentration of 2.8×10^{18} cm^{-3} is required for lasing, and so a fluence of 5.6×10^{14} cm^{-2} is required (assuming that erbium ions are diffused homogeneously by laser reflow).

References

[1] L. He, S. K. Özdemir, J. Zhu, and L. Lang, Phys. Rev. A **82**, 1-4 (2010).
[2] F. Monifi, S. K. Özdemir, and L. Lang, Appl. Phys. Lett. **103**, 1-4 (2013).
[3] L. Chang, X. Jiang, S. Hua, C. Yang, J. Wen, L. Jiang, G. Li, G. Wang, and M. Xiao, Nature Photon. **8,** 524-529 (2014).
[4] B. Min, T. J. Kippenberg, L. Yang, K. J. Vahala, J. Kalkman, and A. Polman, Phys. Rev. A **70**, 1-12 (2004).

Statistical Data

Publications (Apr. 2015 – Mar. 2016)

Journal papers

[1] S. Azami, H. Kudo, Y. Mizumoto, T. Tanabe, J. Yan, and Y. Kakinuma, "Experimental study of crystal anisotropy based on ultra-precision cylindrical turning of single-crystal calcium fluoride," Precision Engineering, Vol. 40, pp. 172-181 (2015).

[2] R. Suzuki, T. Kato, T. Tetsumoto, and T. Tanabe, "Octagoonal toroid microcavity for mechanically robust optical coupling," AIP Advances, Vol. 5, No. 5, 057127 (2015).

[3] T. Tetsumoto, Y. Ooka, and T. Tanabe, "High-Q coupled resonances on a PhC waveguide using a tapered nanofiber with high coupling efficiency," Opt. Express, Vol. 23, No. 12, pp. 16256-16263 (2015).

[4] Y. Ooka, T. Tetsumoto, A. Fushimi, W. Yoshiki, and T. Tanabe, "CMOS compatible high-Q photonic crystal nanocavity fabricated with photolithography on silicon photonic platform," Scientific Reports, Vol. 5, 11312 (2015).

[5] J. Nishimura, M. Kobayashi, R. Saito, and T. Tanabe, "NaCl ion detection using a silica toroid microcavity," Applied Optics, Vol. 54, No. 20, pp. 6391-6396 (2015).

[6] Y. Kakinuma, S. Azami, and T. Tanabe, "Evaluation of subsurface damage caused by ultra-precision turning in fabrication of CaF2 optical micro resonator," CIRP Annals-Manufacturing Technology, Vol. 64, No. 1, 117-120 (2015).

[7] A. C.-Jinnai, W. Yoshiki, and T. Tanabe, "Broad bandwidth pulse propagation through an ultrahigh-*Q* microcavity with a chirped pulse," Jpn. J. Appl. Phys., Vol. 54, No. 12, 12201 (2015).

[8] W. Yoshiki, A. C.-Jinnai, T. Tetsumoto, and T. Tanabe, "Observation of energy oscillation between strongly-coupled counter-propagating ultra-high *Q* whispering gallery modes," Opt. Express, Vol. 23, No. 24, pp. 30851-30860 (2015).

[9] T. Kobatake, T. Kato, H. Itobe, Y. Nakagawa, and T. Tanabe, "Thermal effects on Kerr comb generation in a CaF_2 whispering gallery mode microcavity," IEEE Photonics Journal, Vol. 8, No. 2, 4501109 (2016).

International conferences

[1] S. Tamaki, W. Yoshiki, and T. Tanabe, "Large thermo-optic effects in silica-gold composite toroidal microcavity," The 4th Advanced Lasers and Photon Source (ALPS'15), ALPS5-5, Yokohama, April 22-24 (2015).

[2] Y. Ooka, T. Tetsumoto, A. Fushimi, W. Yoshiki, and T. Tanabe, "Carrier-induced fast all-optical switching in a photonic crystal nanocavity fabricated with a CMOS compatible process," The 4th Advanced Lasers and Photon Source (ALPS'15), ALPSp14-02, Yokohama, April 22-24 (2015). (**best student poster award**)

[3] H. Itobe, Y. Nakagawa, S. Azami, Y. Kakinuma, and T. Tanabe, "Size dependence of thermo-opto-

mechanical oscillation observed in crystalline whispering gallery mode microcavity fabricated with ultra-precision machining," The 4th Advanced Lasers and Photon Source (ALPS'15), ALPSp14-03, Yokohama, April 22-24 (2015). (**best student poster award**)

[4] Y. Nakagawa, T. Kato, and T. Tanabe, "Generation of octave-spanning optical Kerr frequency comb in a dispersion-managed whispering gallery mode microcavity," The 4th Advanced Lasers and Photon Source (ALPS'15), ALPSp14-06, Yokohama, April 22-24 (2015).

[5] Y. Okabe, R. Suzuki, Z. Chen, T. Nagano, T. Kobatake, and T. Tanabe, "Time-domain measurement and noise analysis of a Kerr comb from a toroid microcavity," The 4th Advanced Lasers and Photon Source (ALPS'15), ALPSp14-48, Yokohama, April 22-24 (2015).

[6] T. Kobatake, T. Kato, and T. Tanabe, "Influence of Raman scattering on a Kerr frequency comb generated in a silica toroidal microcavity," The 4th Advanced Lasers and Photon Source (ALPS'15), ALPSp14-49, Yokohama, April 22-24 (2015).

[7] W. Yoshiki and T. Tanabe, "Low-power on-chip all-optical Kerr switch with silica microcavity," CLEO:2015, STu1I.4, San Jose, May 10-15 (2015).

[8] Y. Ooka, T. Tetsumoto, A. Fushimi, W. Yoshiki, and T. Tanabe, "A photolithographic high-Q photonic crystal nanocavity fabricated on a silicon-on-insulator structure," Conference on Laser and Electro-Optics-European Quantum Electronics Conference (CLEO/Europe EQEC 2015), CK-9.2 TUE, Munich, June 21-25 (2015).

[9] T. Tetsumoto, Y. Ooka, A. Fushimi, and T. Tanabe, "Nanocavity formation with a Q of a half-million using photonic crystal waveguide and nanofiber," Conference on Laser and Electro-Optics-European Quantum Electronics Conference (CLEO/Europe EQEC 2015), CK-9.4 TUE, Munich, June 21-25 (2015).

[10] H. Itobe, Y. Nakagawa, A. Azami, Y. Kakinuma, and T. Tanabe, "Fabrication of crystalline WGM microcavity using ultra-precision machining to reveal the size dependence of thermo-opto-mechanical oscillation," Conference on Laser and Electro-Optics- European Quantum Electronics Conference (CLEO/Europe EQEC 2015), CK-9.9 TUE, Munich, June 21-25 (2015).

[11] Z. Chen, T. Nagano, Y. Okabe, T. Kobatake, and T. Tanabe, "Waveform measurement of ultra-high repetition mode-locked pulses generated from a silica toroid microcavity," Progress in Electromagnetics Research Symposium (PIERS 2015), 3A0-15, Prague, 6-9 July (2015).

[12] T. Tanabe, "Optical Kerr switching and comb generation in a silica whispering gallery mode microcavity," Progress in Electromagnetics Research Symposium (PIERS 2015), 3A_14-6, Prague, 6-9 July (2015). (**invited**)

[13] T. Kato, T. Kobatake, Z. Chen, R. Suzuki, and T. Tanabe, "Influence of Raman scattering on Kerr frequency comb in a silica toroidal microcavity," Frontiers in Optics/Laser Science Conference (FiO/LS), FTu2E.4, San Jose, October 18-22 (2015).

[14] S. Tamaki, W. Yoshiki, and T. Tanabe, "Characterization and fabrication of silica-gold composite toroidal optical microcavity," Frontiers in Optics/Laser Science Conference (FiO/LS), San Jose, JW2A.11, October 18-22 (2015).

[15] Y. Nakagawa, T. Kato, W. Yoshiki, Y. Mizumoto, Y. Kakinuma, and T. Tanabe, “Dispersion tailoring of a crystalline whispering gallery mode microcavity for octave-spanning Kerr frequency comb,” Frontiers in Optics/Laser Science Conference (FiO/LS), San Jose, JW2A.32, October 18-22 (2015).

[16] T. Kobatake, T. Kato, H. Itobe, and T. Tanabe, “Temporal cavity soliton generation without laser scan in a crystalline microcavity with negative TO coefficient,” Frontiers in Optics/Laser Science Conference (FiO/LS), JTu4A.45, San Jose, October 18-22 (2015).

[17] M. Kobayashi, J. Nishimura, and T. Tanabe, “pH sensing using a silica toroid microcavity,” Frontiers in Optics/Laser Science Conference (FiO/LS), JTu4A.44, San Jose, October 18-22 (2015).

[18] Y. Ooka, N. A. Daud, T. Tetsumoto, and T. Tanabe, “Efficient electro-optic modulation of a weakly localized resonance in a photonic crystal waveguide,” Frontiers in Optics/Laser Science Conference (FiO/LS), FTu5C.6, San Jose, October 18-22 (2015).

[19] T. Tanabe, T. Kato, T. Kobatake, R. Suzuki, and A. C.-Jinnai “Harmonic mode locking in a high-Q whispering gallery mode microcavity,” SPIE Photonics West, 9727-11, San Francisco, February 13-18 (2016). [Proc. SPIE, Vol. 9727, 97270C (2016).] (**invited**)

[20] T. Tetsumoto, Y. Ooka, and T. Tanabe, “Fiber-coupled photonic crystal nanocavity for reconfigurable formation of coupled cavity system,” SPIE Photonics West, 9756-54, San Francisco, February 13-18 (2016). [Proc. SPIE, Vol. 9756, 97561J (2016).]

[21] W. Yoshiki , A. C.-Jinnai, T. Tetsumoto, S. Fujii, and T. Tanabe, “Time-domain observation of strong coupling between counter-propagating ultra-high Q whispering gallery modes,” SPIE Photonics West, 9727-63, San Francisco, February 13-18 (2016). [Proc. SPIE, Vol. 9727, 97271T (2016).]

[22] R. Suzuki, A. C.-Jinnai, T. Nagano, T. Kobatake, T. Kato and T. Tanabe, “Influence of cavity optomechanics on Kerr frequency combs,” APS March Meeting, A51.00008, Baltimore, March 14 (2016).

Dissertations

Master thesis:

Ryo Suzuki, “Revealing the time and frequency characteristics of Kerr comb”

Syo Tamaki, “Study on the enhancement of optical nonlinearities in a gold doped silica toroid optical microcavity”

Akitoshi Jinnai, “Study on visible optical comb generation by third order optical nonlinearities in a silica toroid optical microcavity”

Tomoya Kobatake, “Theoretical study on the contribution of optical nonlinear effects to the optical Kerr comb”

Yosuke Nakagawa, “Study on the dispersion tailoring by controlling the cross sectional shape of a whispering gallery mode microcavity”

Bachelor thesis:

Hajime Kumazaki, “Study on the coupling between toroid and photonic crystal nanocavities”

Tomohisa Tabata, “Characteristics of photonic crystal nanocavity photodetector fabricated with photolithography”

Naoya Hirota, “Absorption characteristic of a carbon nanotube grown silica toroid microcavity”

Shun Fujii, “Effect of CW-CCW mode coupling on the generation of optical Kerr comb in a toroid microcavity”

Atsuhiro Hori, “Fabrication and investigation towards the laser emission of an Er doped silica toroid microcavity”

Optical measurement of a NIH3T3-cell-adhered microcavity for the cell-cycle analysis applications

Ryusuke Saito (M2)

Sensors based on an ultrahigh-Q optical microcavity have been intensively studied because they have ultrahigh sensitivity and are capable of Label-free sensing. Thus, development of cell-cycle sensor using microcavity will accelerate the study of cell-cycle. In this research, we measured the refractive index of NIH3T3 cells by performance of optical spectrum measurement of a cell-adhered microcavity for the cell-cycle analysis applications.

Key word: Microcavity, sensor, cell-cycle

1. Background

Analysis of the cell cycle has developed greatly in recent years, and various things of cell cycle has been found at the molecular level. In tissues, organs, and solids, it has become clear that cells undergo the influence of various external factors on progression and differentiation of the cell cycle. However, it has not been known how cell cycle progression affects various phenomena such as morphogenesis in development and regeneration, cancer invasion and metastasis. To understand "when, where, and how the cell cycle is controlled in each cell in tissues, organs, and solids" has a very important meaning for not only deepening the understanding of basic biology, but also of medical fields such as cancer research. Furthermore, in basic research to understand the mechanism of differentiation, including regenerative medicine field such as research of iPS cells which Prof. Yamanaka received the Nobel Prize in Physiology or Medicine, to monitor when and how the cell begins differentiation will help further development of regenerative medicine.

In the past, cell cycle progression in living cells and tissues has been analyzed by observation using an optical microscope. The transition from the M phase to the G1 phase of the cell cycle can be discriminated by optical microscopy because morphological changes such as the appearance of chromosomes and mitotic spindles and cell division occur. However, the transition from the G1 phase to the S phase, which is the start of the cell cycle, cannot be identified by optical microscopy because it does not involve morphological changes. In regards to this problem, cell staining using nuclear remodeoxyuridine (BrdU) has been performed, but this method cannot observe live cells in real time. Although research on cell cycle analysis using fluorescence such as Fucci technology has been conducted, cell cycle analysis using fluorescence has a problem in introducing a fluorescent protein by a viral vector, cell cycle and cell properties given by a fluorescent protein. It is impossible to make the no secondary influence on the cell. [1].

Such problems become manifest as, for example, evaluation of fertilized eggs in infertility treatment. It is extremely important to select a fertilized egg that is suitable for returning to the mother infertility treatment, but it is impossible to use the fluorescent protein for the viral vector. Label-free analysis of the cell cycle of a single cell is considered as very useful in such a scene [2,3].

This research aims at providing a new tool for cell cycle research which is an indicator of cell cycle analysis by fluorescent protein. In this research, we will conduct a basic study toward realization of Label-free cell cycle analysis using a silica microcavity that can capture slight changes of the effective refractive index due to environment. Specifically, we aimed at establishing optical measurement technique in liquid using a microcavity, and seeding and adhesion of cells on the microcavity to achieve measurement of its refractive index.

2. Seeding and adhesion of NIH3T3 cells

NIH3T3 cells (mouse embryo fibroblasts) used in this study are ovary fibroblasts of Chinese hamsters, which are established in 1962 and widely used as a standard fibroblast model [4]. This is an immortalized cell and has the property of growing indefinitely like a cancer, although it is a normal cell. In the field of molecular biology, it is easy to observe the intracellular structure in detail because of the formation that spreads flatly.

Also, in wound healing, thanks to the strong polarity of morphology, it is widely used in experiments to study the cytoskeleton rearrangement and cell polarity formation process, which are combined with various gene introductions and RNAi methods. The reason for using NIH3T3 cells in this study is that interaction between cells on the resonator and light in the resonance is expected to be easily coupled due to the fact that the cell division is performed actively and that spreads flat broadly.

Next, the method of cell seeding and adhesion will be explained. (1) Washed the silicon substrate (on which silica microresonators is fabricated) with ethanol and

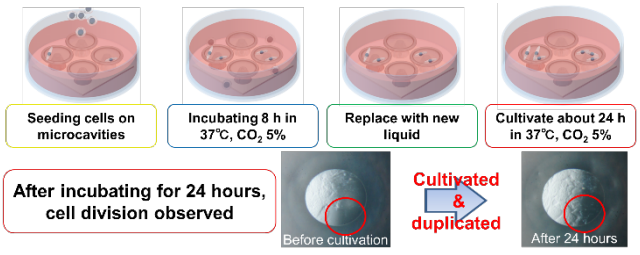

Fig. 1: (upper) Processes of seeding and adhesion of NIH3T3 cells. (bottom) Optical microscope images of toroid microcavities before and after cell adhesion.

sterilized it with ultraviolet rays. Then, NIH3T3 cells are

seeded on the resonator in a medium at 37℃. (2) Cultivated at 37℃ for 8 hours in an environment with a CO_2 concentration of 5% to grow the cells. (3) Carried out seeding and incubation again at 37℃ for 24 hours in an environment of CO_2 concentration of 5% if the cells are not adhered to one microcavity with highly dense. Figure 1 shows optical micrographs before and after cell division on the silica disk microcavity occurred. It was revealed that cell division occurred when a certain degree of cells was mounted on a microcavity.

3. Optical measurement in medium with cells

In this study, it is necessary to measure the optical characteristics of the microcavity in the medium. Therefore, as shown in Fig. 2, we used a pool capable of sinking the substrate and the optical fiber for coupling light. As the result, a quality factor (Q) of 10^4 was measured in the medium that include cells. Here a Q is an evaluation value to represent how long the microcavity confines the light. Next, in order to measure the change of a refractive index due to the presence of cells, the resonance spectrum was measured in air, water, a medium not containing cells, and a medium containing cells. At this time, noise such as temperature, vibration, and light source fluctuation was canceled by using the measurement result of the microcavity placed in the same environment. The change of an effective refractive index Δn is expressed as following equation that includes resonance wavelength shift $\Delta\lambda$:

$$\frac{\Delta\lambda}{\lambda_0} \approx \frac{\Delta n}{n_0} \tag{1}$$

where λ_0 is the resonance wavelength and n_0 is the refractive index of the microcavity. The results obtained from experiment and Eq. (1) are summarized in Table 1. From these results, refractive index difference between the medium and water Δn_{med} and refractive index change due to the existence of cells are

$$3.00 \times 10^{-4} \leq \Delta n_{\mathrm{med}} \leq 3.678 \times 10^{-4}, \tag{2}$$

$$9.7 \times 10^{-4} \leq \Delta n_{\mathrm{cell}} \leq 12.4 \times 10^{-4}. \tag{3}$$

As a result of the above, it was possible to measure the refractive index with a resolution of the order of 10^{-4} in liquid environment.

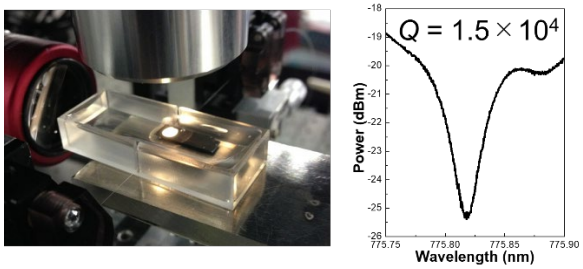

Fig. 2: (left) Experimental setup of optical measurement in liquid environment. (right) Resonance spectrum measured in medium that includes cells.

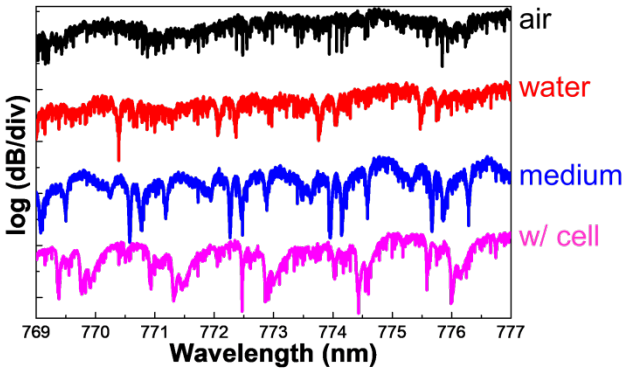

Fig. 3: Resonant spectra in different environments.

Table 1: Shifts of resonance wavelength and effective refractive index, and typical Q in different environments.

	$\Delta\lambda$	Δn	Q (Typ.)
In air	-	-	1.0×10^5
In water	0	0	8.3×10^3
In medium (w/o cell)	165.1±50.0 pm	$(3.3\pm0.4)\times10^{-4}$	5.4×10^3
In medium (w/ cell)	588.3±3.5 pm	$(1.1\pm0.4)\times10^{-3}$	1.5×10^4

4. Conclusion

By sequentially tracking the refractive index change of the cell, we clarified the relation between cell peripheries and change in refractive index of cells. In addition, we got the following results toward the final goal of analyzing the cell-cycle in real-time and label-free. (1) Cells were seeded and adhered onto a silica microcavity. (2) We realized an experimental system of optical measurement in label-free medium at real-time using a silica microcavity with cells. (3) By canceling the fluctuation of the measurement system using a silica microcavity, the influence of the change in the refractive index due to the medium and cells were measured at the order of 10^{-4}.

References

[1] L. Wanga, *et al.*, Science Direct **25**, 990-995 (2010).
[2] F. Vollmer and S. Arnold, Nat. Methods **5**, 591-596 (2008).
[3] F. Vollmer, *et al.*, PNAS **105**, 20701-20704 (2008).
[4] 秋山徹，河府和義(編)，“細胞・培地活用ハンドブック”羊土社.